

9

Multidimensional PGSE NMR

Much of high-resolution NMR spectroscopy derives its power from the abundance of information present in the spectrum, that distribution of frequencies associated with the evolution of spin phase in the presence of molecular-based interactions, such as the chemical shift, the scalar couplings, and the dipolar and quadrupole interactions. These spectra are usually Fourier conjugates, with respect to time, of oscillatory signals acquired as a function of time or, in the case of multidimensional NMR, arising from spin magnetisation that has previously evolved in a well-defined and prior time domain.

Oscillatory data are naturally analysed using such Fourier transformation. This book deals with the additional spin phase evolution associated with translational displacements under the influence of time-varying magnetic field gradients. These phase evolutions may also induce oscillatory behaviour in the signal, for example where flow is present, and Fourier transformation in this case yields the spectrum of molecular displacements. However, as we have seen, when the molecular ensemble is characterised by diffusive displacements, the pulsed gradient induced phase-spreading results not in an oscillatory signal, but one exhibiting exponential decay with respect to the squared gradient pulse area, q^2 . Fourier transformation with respect to q results in a spectrum of displacement Z , a Gaussian the width of which is determined by the molecular diffusion coefficient, D , just as spin–spin relaxation results in a signal which decays with time and the Fourier conjugate with respect to time of which is a frequency spectrum, the width of which is determined by the relaxation time T_2 . Of course we could easily analyse those spectra by measuring their widths to find the values of D or T_2 .

But suppose the molecular ensemble featured a plethora of sub-ensembles exhibiting different diffusion coefficients or relaxation times. This would result in a multi-exponential signal and spectra comprising a superposition of Gaussians representing each sub-ensemble. Such a superposition would be very hard to analyse since each sub-ensemble would contribute to the overall width and we would need to apply a fitting process involving an unknown number of Gaussians. Of course, the problem is we have simply calculated the wrong ‘spectrum’. What we really needed was not the spectrum of displacements or frequencies in each respective case, but instead the spectrum of diffusion coefficients or relaxation times. The type of processing that generates these from multi-exponential decays is known as an inverse Laplace transformation.

As we will see in this chapter, both Fourier transformation and inverse Laplace transformation can be used in conjunction with PGSE NMR as a basis for a multi-dimensional characterisation, whether as separation, correlation, or exchange experiments. And having incorporated inverse Laplace transformation, we may introduce relaxation effects to provide additional dimensions. In a porous medium, molecular

migration may also result in changes in local relaxation rates, which depend upon pore size, or in diffusion coefficient, another parameter sensitive to local pore geometry. Such changes will be manifest in exchange experiments, in which we correlate identical parameters measured on the same spin coherences, but at times separated by a mixing period τ_m . Equally we may find it helpful to correlate differing NMR parameters obtained as close as possible in time, in other words as $\tau_m \rightarrow 0$. For example, $D - T_2$ maps give us insight regarding the correlation of translational and rotational mobility of molecules. Even the simplest of all NMR experiments, the measurement of the spectrum associated with the FID, yields vital information regarding molecular translational motion. In porous materials, spins in migrating liquid molecules experience local susceptibility-related magnetic fields, which fluctuate as the molecules move about, leading to changes in the NMR spectrum.

This chapter takes us through the various Fourier and Laplace dimensions in which molecular translation plays a role. At the heart of the methods described here is the concept of multiplexing, the encoding of our signal in multiple independent dimensions. In mathematical terms, this simply means that instead of acquiring a signal as a function of one experimental variable, we acquire it as a function of two or more. First, however, we compare the nature of the transformations.

9.1 Fourier or Laplace?

9.1.1 An example from PGSE NMR

Suppose an ensemble of molecules is described by sub-ensembles weighted by probability density $P(D)$, each with diffusion coefficient, D . Then the q -space signal acquired in a narrow gradient pulse PGSE NMR experiment as shown in Fig. 9.1(a) will be the integral over the sub-ensembles

$$E(q) = \int P(D) \exp(-q^2 D \Delta) dD \quad (9.1)$$

with Fourier conjugate $\mathcal{F}\{E\}$ with respect to q given by

$$\bar{P}(Z) = \int P(D) (2\pi D \Delta)^{-1/2} \exp(-Z^2 / 2D \Delta) dD \quad (9.2)$$

In this transformation, a multi-exponential decay in q^2 has been replaced by a sum of Gaussian propagators. An example is shown in Fig. 9.1(b), where the ensemble consists of the simplest possible non-trivial example with one sub-ensemble comprising two-thirds of the molecules with diffusion coefficient D_1 and another sub-ensemble comprising one-third of the molecules with diffusion coefficient D_2 . For convenience we take $D_2 = 4D_1$. In Fig. 9.1(b), the two distinct Gaussians are barely discernable. What we seek is a different type of transformation that returns $P(D)$ directly so as to reveal the distribution of diffusion coefficients shown in Fig. 9.1(c).

9.1.2 Forward and inverse

Consider the following two pairs of equations.

$$\begin{aligned} f(\omega) &= \mathcal{F}^{-1}\{S(t)\} = (2\pi)^{-1/2} \int_{-\infty}^{\infty} \exp(i\omega t) S(t) dt \\ S(t) &= \mathcal{F}\{f(\omega)\} = (2\pi)^{-1/2} \int_{-\infty}^{\infty} \exp(-i\omega t) f(\omega) d\omega \end{aligned} \quad (9.3)$$

and

$$\begin{aligned} f(R) &= \mathcal{L}^{-1}\{S(t)\} \\ S(t) &= \mathcal{L}\{f(R)\} = \int_0^{\infty} f(R) \exp(-Rt) dR \end{aligned} \quad (9.4)$$

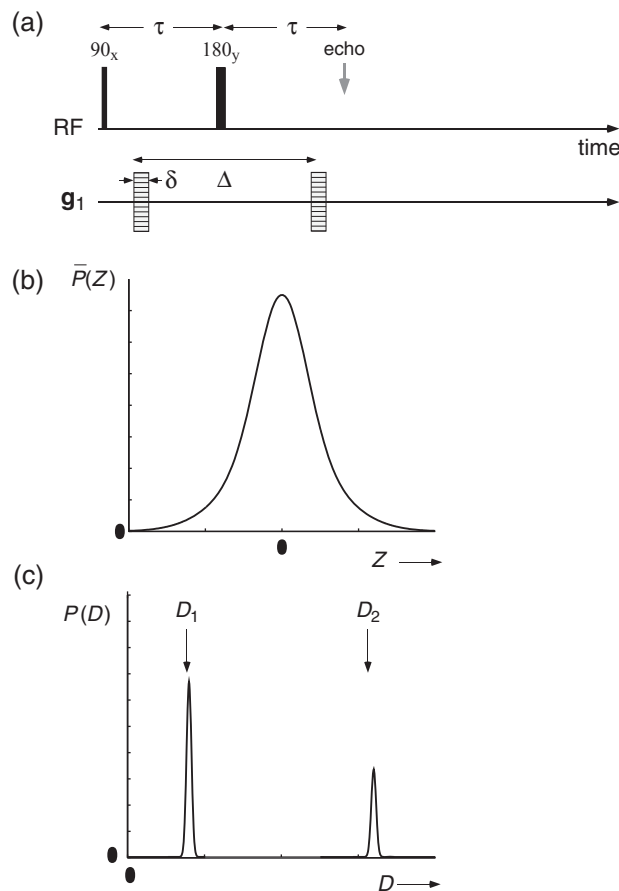


Fig. 9.1 One-dimensional PGSE NMR in which a gradient pulse pair, \mathbf{g} , encodes the echo.
 (a) Basic 1-D pulse sequence. (b) The result of Fourier transforming the signal with respect to q when the molecular ensemble exhibits two different diffusion coefficients. A propagator is returned comprising two Gaussians co-centred at zero displacement but with different widths.
 (c) The result when the signal is inverse Laplace transformed to reveal the two diffusion coefficients directly.

Note that eqn 9.4 may be rewritten to encompass the PGSE NMR result of eqn 9.1,

$$\begin{aligned} P(D) &= \mathcal{L}^{-1}\{E(q^2\Delta)\} \\ E(q^2\Delta) &= \mathcal{L}\{P(D)\} = \int_0^\infty P(D) \exp(-q^2 D \Delta) dD \end{aligned} \quad (9.5)$$

The first pair represent the inverse and forward Fourier transformations familiar in NMR spectroscopy and MRI. They are symmetric, well-defined, and easily implemented digitally using the FFT algorithm. The second (or third) pair is of particular interest here. The second of the two equations represent the multi-exponential decay in which $f(R)$ is the probability of finding a decay rate R . This integral is known as the Laplace transformation and its outcome, in which $f(R)$ is ‘transformed’, is the time-domain signal $S(t)$, such as might be found in an NMR relaxation experiment. Its inverse, indicated in the first of the two equations, takes $S(t)$ to $f(R)$ and enables us to calculate the relaxation rate distribution from a knowledge of the NMR signal. This ‘inverse Laplace transformation’ (ILT) may be desirable, but unlike the Fourier inverse is asymmetric, ill-defined, and not at all easily implemented.

9.2 Inverse Laplace transformations

9.2.1 Analytic and numerical inverse Laplace transformations

There does exist an analytic form to the inverse Laplace transformation of eqn 9.4. In particular, it is the contour integral in the complex plane [1]

$$f(R) = \mathcal{L}^{-1}\{S(t)\} = \frac{1}{2\pi i} \int_{\gamma-i\infty}^{\gamma+i\infty} S(t) \exp(Rt) dt \quad (9.6)$$

where γ is a vertical contour positioned to the right of any singularities. Numerically, this integral is unhelpful, since the need to multiply by a potentially increasing large exponential $\exp(Rt)$ can lead to exponential divergence of numerical solutions due to noise in $S(t)$ and finite precision errors. The inverse Laplace transform is therefore an ill-posed problem.

The Laplace transform belongs to a class of integrals known as ‘Fredholm integrals of the first kind’ [1, 2], of the form

$$S(t) = \int_a^b K(t, R) f(R) dR \quad (9.7)$$

where $K(t, R)$ is known as the kernel. The standard problem is, given a knowledge of the kernel and the signal $S(t)$, how do we find $f(R)$? Because this question is ill-posed, it requires a special approach.

Suppose we discretise the problem and write the signal to be inverted, $S(t)$, as a vector arising from the discrete sampling times, t_i , where $i = 1 \dots N$, with the solution $f(R)$ being discretised in the domain of R_j where $j = 1 \dots M$. If we pre-specify the

values of R_j to be used, then we may calculate *a priori* the $N \times M$ kernel matrix $K_{ij} = K(t_i, R_j)$ and

$$S(t_i) = \sum_{j=1}^M K(t_i, R_j) f(R_j) \quad (9.8)$$

or

$$\underline{S} = \underline{K} \underline{f} \quad (9.9)$$

In fact, when we are dealing with measurement, we need to take account of noise. For example, each $S(t_i)$ value will have some noise ϵ_i , so that strictly we should write eqn 9.9 as

$$\underline{S} = \underline{K} \underline{f} + \underline{\epsilon} \quad (9.10)$$

At first, we might be tempted to think that we could solve for \underline{f} by using the pseudo-inverse $\underline{\underline{K}}^{-1}$ of the matrix $\underline{\underline{K}}$ so that

$$\underline{f} = \underline{\underline{K}}^{-1} \underline{S} \quad (9.11)$$

or again, including the noise, by

$$\underline{f} = \underline{\underline{K}}^{-1} \underline{S} + \underline{\underline{K}}^{-1} \underline{\epsilon} \quad (9.12)$$

The pseudo-inverse is calculated by writing $\underline{\underline{K}}$ as a product of an orthogonal¹ $N \times N$ matrix $\underline{\underline{U}}$, a diagonal $N \times M$ matrix $\underline{\underline{\Sigma}}$, and an orthogonal $M \times M$ matrix $\underline{\underline{V}}$ as

$$\underline{\underline{K}} = \underline{\underline{U}} \underline{\underline{\Sigma}} \underline{\underline{V}} \quad (9.13)$$

a process known as singular value decomposition. The diagonal values of $\underline{\underline{\Sigma}}$ are known as the singular values of $\underline{\underline{K}}$. The pseudo-inverse of $\underline{\underline{K}}$ is obtained by writing

$$\underline{\underline{K}}^{-1} = \underline{\underline{V}}^{-1} \underline{\underline{\Sigma}}^{-1} \underline{\underline{U}}^{-1} \quad (9.14)$$

where $\underline{\underline{\Sigma}}^{-1}$ is obtained by taking the inverse of all the diagonal elements in $\underline{\underline{\Sigma}}$. While in principle $\underline{\underline{K}}^{-1}$ may be calculated numerically, the matrix $\underline{\underline{K}}$ is ‘ill-conditioned’. This is reflected in the large value of the condition number, defined by the product of the norms $\|\underline{\underline{K}}\| \cdot \|\underline{\underline{K}}^{-1}\|$.² The condition number gives the maximum ratio of the fractional error in the solution \underline{f} to the fractional error in \underline{S} . A large condition number means that the inversion process tends to have an explosive effect on any errors, $\underline{\epsilon}$, in \underline{f} .

There is another sense in which the inverse problem is ill-posed for the Fredholm integral eqn 9.7. Suppose we add to a solution $f(R)$, the oscillatory function $\sin(\omega R)$, then the Riemann–Lebesgue lemma [3] states that for any $K(t, R)$ there exists a frequency ω such that

$$\int_a^b K(t, R) \sin(\omega R) dR = 0 \quad (9.15)$$

This means that for an arbitrarily large amplitude A and for arbitrarily small errors ϵ in $S(t)$, if $f(R)$ is a solution to eqn 9.7, then there exists a frequency ω such that

¹An orthogonal matrix $\underline{\underline{U}}$ is one for which $\underline{\underline{U}}^T = \underline{\underline{U}}^{-1}$.

²The Frobenius norm of a matrix $\underline{\underline{K}}$ is defined as $\|\underline{\underline{K}}\| = \sqrt{\text{Trace}(\underline{\underline{K}} \underline{\underline{K}}^*)}$ or $\sqrt{\sum_i \sum_j K_{ij}^2}$. For comparison, the Euclidean norm of a vector, \underline{x} is $\|\underline{x}\| = \sqrt{\sum_i x_i^2}$.

condition number

$f(R) + A \sin(\omega R)$ is also a solution within that error ϵ . That is a recipe for an infinite solution set! Whichever way we invert this problem, using a measurement of $S(t)$ to obtain an estimate for $f(R)$, there is no unique solution. Another approach is needed in which additional criteria are imposed.

9.2.2 Regularised non-negative least squares in 1-D

A practical approach to the Laplace transform inversion was proposed by Stephen Provencher in 1982 [4]. First, we write down the integral equation in discrete form, allowing for noise in the signal

$$S(t_i) = \sum_{j=1}^M \exp(-t_i R_j) f(R_j) + \epsilon_i \quad (9.16)$$

Absolute prior knowledge is then applied by requiring that each spectral amplitude, $f(R_j)$, is positive. Statistical prior knowledge is applied by requiring an optimal, minimum mean-squared error solution to be found. And finally, the principle of parsimony requires that we use the simplest solution, the one that contains the least detail or information not already expected. This last point deals with the Riemann–Lebesgue problem, by requiring that our solution be as ‘smooth’ as possible in the variable R .

Tikhonov regularisation

Provencher implemented parsimony using a method known as Tikhonov regularisation [5]. The idea is as follows: suppose we attempt a least-squares solution \underline{f} to eqn 9.9. Then the residual is $\|\underline{K}\underline{f} - \underline{S}\|^2$, the quantity we would seek to minimise. Tikhonov regularisation adds a term $\underline{\Gamma}\underline{f}$ in the minimisation process so that the residual to be minimised is $\|\underline{K}\underline{f} - \underline{S}\|^2 + \alpha^2 \|\underline{\Gamma}\underline{f}\|^2$, where α^2 is known as the regularisation parameter. The operator, Γ , is chosen on the basis of parsimony, that is to favour smoothness with minimum number of peaks. One such smoothness operator might involve the curvature of $f(R)$ so that

$$\|\underline{\Gamma}\underline{f}\|^2 = \int_{R_{min}}^{R_{max}} [f''(R)]^2 dR \quad (9.17)$$

where (R_{min}, R_{max}) represent the bounds of the solution variable R . Hence a standard way of expressing the solution is

$$\begin{aligned} V(\alpha) &= \|\underline{K}\underline{f} - \underline{S}\|^2 + \alpha^2 \|\underline{\Gamma}\underline{f}\|^2 \\ &= \text{minimum} \end{aligned} \quad (9.18)$$

The way to proceed numerically is as follows [4]. We start with the signal vector \underline{S} , the elements of which, S_j , correspond to each sampling value (for example time value) labelled t_i , where $i = 1\dots N$. Next, we choose *a priori* a range in the solution space of discrete relaxation rates R_j , where $j = 1\dots M$. The solution vector \underline{f} , the ‘spectrum of relaxation rates’, has values corresponding to each R_j and labelled by f_j with $j = 1\dots M$. Thus the solution satisfies

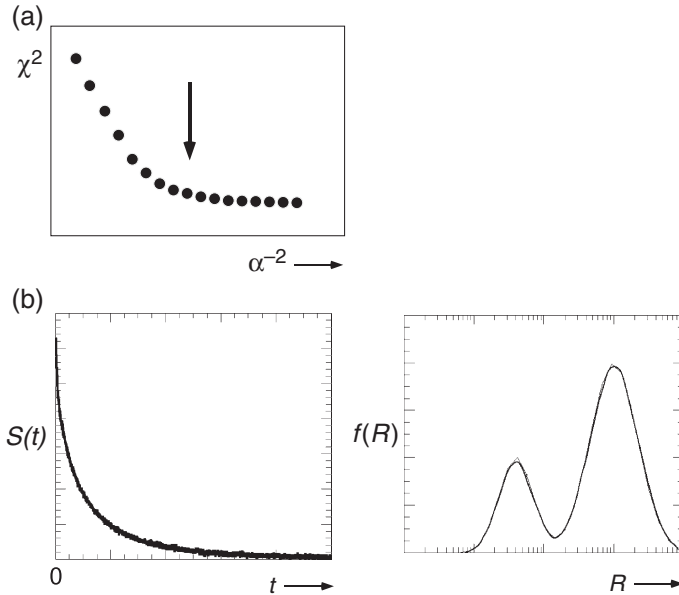


Fig. 9.2 Numerical inverse Laplace transform of time-domain signal $S(t)$ decaying as a multi-exponential, along with spectrum of relaxation rates, $f(R)$. (a) Adjustment of the regularisation parameter α^2 to just minimise χ^2 , the arrow showing the chosen value, while (b) and (c) show $S(t)$ and $f(R)$, respectively, with the latter calculated using a logarithmic spacing of R values.

$$\begin{aligned} V(\alpha) &= \sum_i^N \sum_j^M (S_i - \exp(-t_i R_j) f_j)^2 + \alpha^2 \sum_j^M (2f_j - f_{j+1} - f_{j-1})^2 \\ &= \text{minimum} \end{aligned} \quad (9.19)$$

where the last term contains the numerical form of the second derivative of $f(R)$. With the f_j values constrained to be positive, the least squared minimisation is carried out using a range of α values, and the residual $\chi^2 = \sum_i^N \sum_j^M (S_i - \exp(-t_i R_j) f_j)^2$ calculated for each α^2 . By the principle of parsimony, a value of α^2 is chosen (see Fig. 9.2(a)) which minimises χ^2 , but only just. Such a solution, when we minimise according to eqn 9.19, has the least degree of curvature needed to well represent the data. The programme developed by Provencher to carry out this 1-D ILT process is known as CONTIN [6], since it allows, in effect, a continuous distribution of relaxation rates to be determined. The method was soon after applied to the analysis of NMR relaxation data [7].

Binning, integration, and resolution

Note that the R_j may be linearly spaced but, more commonly, we might chose them spaced equally in $\log(R)$, so that a wide range of decades can be covered without the need for an excessively large value of M . In operating the algorithm, these pre-assigned R_j are essentially ‘bins’ in a histogram chosen to represent the data. In that sense they

are discrete and their intensity correctly represents the total probability of finding the relaxation rate in the range defined by adjacent bins. To re-emphasise, the binned intensities are correctly normalised however we choose our binning scale. By contrast, in a continuum representation, one needs a conversion correction (a $d \log(R) = R^{-1}dR$ weighting) in transferring from a logarithmic scale to a linear scale.

Figure 9.2(b) and (c) show an example of noisy, time-domain data undergoing multi-exponential decay, transformed using the Tikhonov regularised least squares process of Provencher. Note the finite width of the peaks in the spectra, characteristic of solutions regularised by curvature according to the parsimony condition. Typically, such broadening means that the method cannot easily resolve relaxation rates less than a factor of three in separation.

Inversion robustness

The quality of the ILT algorithm can best be judged by subjecting the process to data generated from a known spectrum of relaxation times. Prange and Song [8] have demonstrated the degree of consistency available in such a test by using an known bimodal distribution of 100 T_2 values logarithmically spaced between 0.001 and 10 s, as shown in Fig. 9.3(a). From this they generate an echo decay train consisting of 8192 points spaced by of 0.0002 s, starting at 0.0002 s, adding Gaussian noise with standard deviation is 0.025 of the maximum echo value. They then subject this to a non-regularised NNL inversion, resulting in a ‘three delta function’ solution, and to a regularised inversion, from which a smooth distribution is obtained, closely, but not exactly, resembling the *a priori* spectral distribution. Most importantly, they demonstrate the effect of the noise by re-analysing the data using a different noise realisation based on the same standard deviation and Gaussian distribution. The results are encouragingly similar but, as Prange and Song show in their article, as the noise standard deviation increases, so does the variability of the solution space.

9.2.3 Regularised non-negative least squares in 2-D

Having seen that it is possible to invert multi-exponential data in 1-D, we now turn to 2-D data sets. Because Fourier transforms are linear operations, we may independently transform 2-D data sets along either axis, and in either order, in a well-defined manner. The non-linear inverse Laplace transformation offers no such luxury, and any attempt will founder because of the dependence on the chosen order of transformation directions, and the sensitivity to noise of the outcome on the edges of peaks in the 2-D spectrum. Instead the regularised non-negative least squares approach must be applied to the 2-D data set taken as a whole.

Suppose we acquire a signal in two independent dimensions, both of which exhibit multi-exponential decay. Examples might be $T_1 - T_2$ or $T_2 - D$ experiments. For convenience consider the latter, where the signal $S(t_i, q_j^2)$ is dependent on both time t_i , where $i = 1 \dots N_1$ and wavevector-squared q_j^2 , where $j = 1 \dots N_2$ as

$$S(t_i, q_j^2) = \sum_{k=1}^{M_1} \sum_{l=1}^{M_2} \exp(-t_i R_k) \exp(-q_j^2 \Delta D_l) f(R_k, D_l) + \epsilon_{i,j} \quad (9.20)$$

or

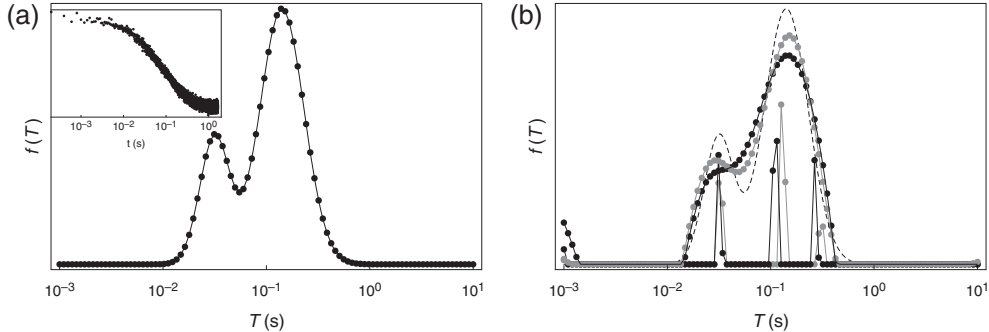


Fig. 9.3 (a) *A priori* T_2 spectrum used to synthesise the echo decay data shown in the inset. The noise standard deviation is 0.025 of the maximum echo value. (b) T_2 spectra obtained by NNLS (these are the ‘spiky’ results that are scaled to 10% to fit on the plot) along with the smooth regularised T_2 spectral solution. The black and grey dots are two independent solutions for the data shown in (a) but with a different noise realisation at the same standard deviation. The original T_2 spectrum (dashed curve) is shown for comparison. (Reproduced by permission from Prange and Song [8].)

$$\underline{\underline{S}} = \underline{\underline{K}_1} \underline{\underline{f}} \underline{\underline{K}_2} + \underline{\underline{\epsilon}} \quad (9.21)$$

where $K_{1i,k} = \exp(-t_i R_k)$ and $K_{2l,j} = \exp(-q_j^2 \Delta D_l)$. We seek the 2-D spectrum $\underline{\underline{f}}$ with elements $f(R_k, D_l)$ such that $k = 1 \dots M_1$ and $l = 1 \dots M_2$. Equation 9.21 involves the multiplication of $N_1 \times M_1$, $M_1 \times M_2$, and $M_2 \times N_2$ matrices. Of course, it is possible to re-express this equation making $\underline{\underline{S}}$ and $\underline{\underline{f}}$ vectors rather than tensors, thus transforming the 2-D character of the equation to a 1-D character as in the original Provencher form of eqn 9.10. All we would have to do is to rewrite the successive rows of matrices $\underline{\underline{S}}$ and $\underline{\underline{f}}$ as a concatenated string of vectors, at the same time appropriately transforming the kernel matrices, $\underline{\underline{K}_1}$ and $\underline{\underline{K}_2}$, to make a single outer product matrix, $\underline{\underline{K}_0} = \underline{\underline{K}_1} \otimes \underline{\underline{K}_2}$, involving appropriately concatenated exponential decays. We could then apply the 1-D regularised non-negative least squares process described earlier. These new vectors would be large, of dimension $N_1 \times N_2$ and $M_1 \times M_2$, respectively. Consequently the demands on computation time would be severe. Worse, the dimension of $\underline{\underline{K}_0}$ is enormous, being $N_1 \times M_1 \times M_2 \times N_2$. To store this matrix requires a great deal more memory than storing the individual $\underline{\underline{K}_1}$ and $\underline{\underline{K}_2}$ matrices. The method is impractical as it stands.

A nice solution to problem has been demonstrated by Venkataramanan *et al.* [9]. Their procedure involves first reducing the dimension of the matrices by singular value decomposition. In this process the matrices are reorganised by unitary transformations so that the singular values along the diagonal are ordered by decreasing size, the matrix dimension being truncated once the singular values become sufficiently small, with typically 30 or so of the largest being retained. That process, in itself, represents a subtle form of regularisation. Then, these smaller dimension matrices are projected

as vectors and the 1-D regularised non-negative least squares solution obtained, the solution being finally reorganised into the desired 2-D array.

9.2.4 Testing using known distributions and pearling effects

The ill-defined nature of the inverse Laplace transformation demands that some caution be applied when using it. But like all ‘black boxes’, the inner workings of which have an element of mystery, the performance of the ILT may be judged on what it does to data the inverse of which is known *a priori*.

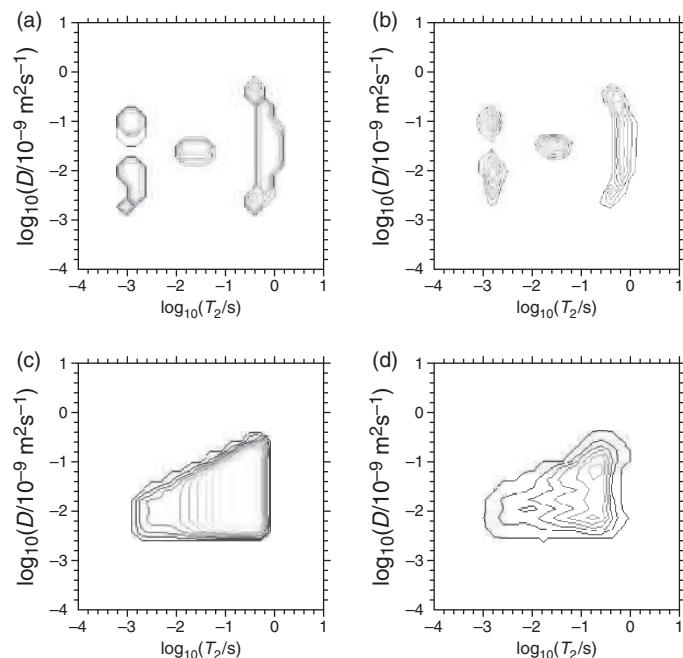


Fig. 9.4 Numerical 2-D inverse Laplace transforms (b and d) of signals generated using known precursor $D - T_2$ distributions (a and c) in which the signal-to-noise ratio is 10^4 . Calculations were carried out by Daniel Polders.

The test is straightforward. We generate some chosen distribution of decay rates, calculate the expected signal, add some noise, and then run the result through the transformation to see if we generate that with which we started. Figure 9.4 provides an example of such a procedure in the case of a 2-D ILT. The known distributions, $f(R, D)$, here chosen as $D - T_2$ correlations in which each pixel represents a diffusion and T_2 component, scaled by its intensity, are generated as 100×100 matrices, in (a) as a ‘smiley face’ and in (c) as a trapezium of ramped intensity. The decaying signals, $S(t, q^2)$, were calculated using eqn 9.20, the gradient strength, G , being ramped from 0 to 1 T m^{-1} in 49 logarithmically spaced steps, with the time, t varied from 2 ms to 2000 ms in steps of 1 ms, corresponding to a PGSE experiment followed by a CPMG

train, in which $\tau = 250\ \mu\text{s}$ and in which every second echo is collected. The added Gaussian noise is such that the signal-to-noise ratio for $S(t, q^2)$ is 10^4 at the signal origin.

Figure 9.4(d) illustrates a curious effect found in the regularised ILT solution, namely a tendency to convert flat distributions into ‘lumpy’ distributions. The smoothly ramped trapezoidal distribution used to calculate the input data is represented in the inversion process by a distribution of similar boundary shape, but in which the intensity is no longer smoothly ramped but gathered into local ‘islands’ of intensity. This effect is commonly termed ‘pearling’. Pearling is clearly an artifact of the transformation, but occasionally useful despite that. For example, suppose that one is to quantitatively analyse parts of a continuous distribution. It has the effect of ‘lumping’ intensity into localised regions, ‘bins’ of intensity that may be independently integrated.

Sections 9.4 and beyond will present examples of the inverse Laplace transformation in action. But we begin our discussion of multi-dimensional PGSE NMR with a survey of methods confined to Fourier space.

9.3 Multi-dimensional Fourier–Fourier methods

Both k -space and q -space are traversed by the use of magnetic field gradient pulses, with Fourier transformation taking us respectively to the domains of molecular position \mathbf{r} and molecular displacement \mathbf{R} . One obvious type of multidimensional Fourier–Fourier application concerns the combination of k -space and q -space encoding to produce an image with voxels endowed with a ‘displacement contrast’, in its most complete form with the propagator for displacement being measured for each image element. We term this experiment ‘dynamic NMR microscopy’ and devote the next chapter to its description. In this chapter, however, we shall be concerned only with multidimensional methods where imaging is treated as a separate and independent contrast. Where imaging is not performed, and this will be the usual case here, the experiments to be discussed apply to the whole sample. Should the multidimensional encoding methods discussed in this chapter be concatenated with a further image encoding, an ambitious expansion into further dimensions, then we can consider that the experiments discussed here apply to one image volume element or voxel. Of course there are only so many NMR dimensions we can practically employ, each one requiring a further multiplexing and further dedication of acquisition time. Two or three seems reasonable. We shall, in this chapter, be content to use those up in the service of q -space alone!

9.3.1 VEXSY

Consider an ensemble of molecules that exhibit a propagator $\bar{P}(\mathbf{R}, \Delta)$, and which are subject to the pulse sequence shown in Fig. 9.1 in which two separate pairs of short duration PGSE gradients, \mathbf{g}_1 and \mathbf{g}_2 , independently encode the spin phase, engendering phase shifts $\exp(i\mathbf{q}_1 \cdot \mathbf{R}_1 + i\mathbf{q}_2 \cdot \mathbf{R}_2)$ for molecules that migrate \mathbf{R}_1 along the gradient direction over the first pair and \mathbf{R}_2 over the second pair. Following the first 90° RF pulse, the transverse magnetisation is phase-encoded according to the displacement \mathbf{R}_1 , which occurs over the duration Δ between the first PGSE pulse

pair. Following a mixing time delay τ_m , spins associated with molecules displaced by \mathbf{R}_1 during the first phase-encoding period will have moved to a different part of the displacement spectrum, $\bar{P}(Z, \Delta)$. In other words, there exists a conditional probability distribution $\mathcal{P}(\mathbf{R}_1, \Delta | \mathbf{R}_2, \Delta; \tau_m)$, which is assumed to be common to the entire molecular ensemble. It tells us the likelihood that a molecule that moved by \mathbf{R}_1 over the time delay Δ will be displaced by \mathbf{R}_2 over Δ , when this latter measurement is made after a mixing delay τ_m . We may thus write down the final, normalised (to zero gradient) phase-encoded echo signal as

$$E(\mathbf{q}_1, \mathbf{q}_2, \tau_m, \Delta) = \iint \bar{P}(\mathbf{R}_1, \Delta) \mathcal{P}(\mathbf{R}_1, \Delta | \mathbf{R}_2, \Delta; \tau_m) \times \exp(i\mathbf{q}_1 \cdot \mathbf{R}_1 + i\mathbf{q}_2 \cdot \mathbf{R}_2) d\mathbf{R}_1 d\mathbf{R}_2 \quad (9.22)$$

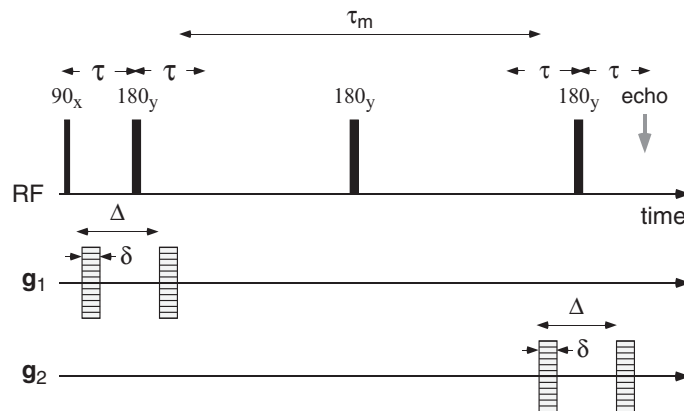


Fig. 9.5 RF and gradient pulse sequence for velocity exchange spectroscopy (VEXSY) in which successive PGSE pulse pairs (\mathbf{g}_1 , and \mathbf{g}_2) are applied separated by a delay time τ_m . To be an effective exchange experiment in which like phenomena are compared at different times, \mathbf{g}_1 and \mathbf{g}_2 are required to be in the same direction.

The 2-D experiment, known as VEXSY [10], for velocity exchange spectroscopy, is performed by encoding the signal in the two independent \mathbf{q} domains. It is an exchange experiment because the molecular displacements or velocities are probed at different times to see if they have changed. To be an exchange experiment, we need to be comparing the same parameter measured at different times. That means, in effect, that the two gradient pulses should be applied in the same direction, so that following a 2-D inverse Fourier transformation, we compare displacements Z_1 and Z_2 along the same axis, but at different times.³ Equation 9.22 tells us that the spectrum returned following the 2-D FT with respect to q_1 and q_2 is the joint probability distribution

$$\bar{P}_2(Z_1, \Delta; Z_2, \Delta; \tau_m) = \bar{P}(Z_1, \Delta) \mathcal{P}(Z_1, \Delta | Z_2, \Delta; \tau_m) \quad (9.23)$$

³The experiment in which the gradient \mathbf{g}_1 and \mathbf{g}_2 are not parallel is discussed in Section 9.3.4.

For very short mixing times, such that the molecules have not had the chance to move to a different sub-ensemble, $\mathcal{P}(Z_1, \Delta | Z_2, \Delta; \tau_m)$ will be a delta function $\delta(Z_1 - Z_2)$, and the distribution will be diagonal, albeit broadened by diffusion over the time Δ . When the mixing time is very long compared with any characteristic time for the ensemble, $\mathcal{P}(Z_1, \Delta | Z_2, \Delta; \tau_m)$ will be independent of Z_1 and return to the *a priori* propagator $P(Z_2, \Delta)$. This latter situation always applies for the case of Brownian motion of small molecules where collision times are picoseconds. The VEXSY experiment simply returns a 2-D spectrum that is a product of two Gaussians, as shown in Fig. 9.6.

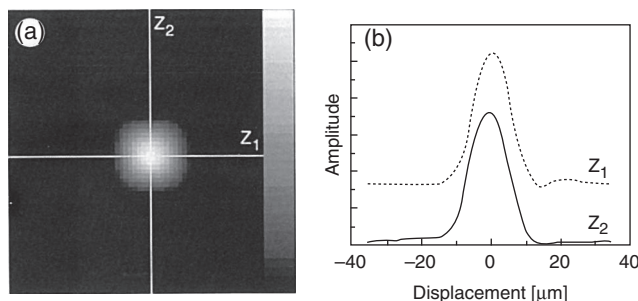


Fig. 9.6 (a) 2-D VEXSY spectrum, $\bar{P}_2(Z_1, \Delta | Z_2, \Delta; \tau_m)$, for unrestricted Brownian motion of water molecules and (b) orthogonal slice profiles shown the independent Gaussian displacement spectrum associated with each encoding. (Reproduced with permission from reference [10].)

For flow in a porous medium, where characteristic ensemble exchange times, τ_v , may be made comparable with the mixing time τ_m , the structure of the VEXSY spectrum is considerably more interesting. Figure 9.7 [11] shows displacement propagators⁴ obtained from water flowing in a 0.5-mm diameter (d) bead pack, at a variety of encoding times Δ . In this example, the mean velocity $\langle v \rangle$ is 24 mm s^{-1} , $\tau_v = d/\langle v \rangle = 21 \text{ ms}$, and $Pe = 5600$. Note that as Δ is made comparable to, and then larger than, τ_v , the distribution of velocities moves towards a Gaussian. Note that it is customary to step q -space over both positive and negative values in order to obtain the best quality representation of the propagator following Fourier transformation.

Figure 9.8 shows the evolution of the joint probability density $\bar{P}_2(Z_1, \Delta | Z_2, \Delta; \tau_m)$ (plotted in velocity units) for the 0.5-mm diameter bead pack, at $Pe = 1900$. A range of mixing times are shown, from $\tau_m \ll \tau_v$ to $\tau_m \gg \tau_v$. In the figure labels, $\tau'_m = \tau_m + \Delta$ is used to provide a more accurate measure of the total mixing time. For negligible mixing time, the velocity distribution is expected not to change between the first and the second encoding interval, leading to intensities along the main diagonal. Some broadening is present because of diffusive motion during Δ . For τ_m comparable with τ_v , significant off-diagonal intensity indicates velocity changes. Figure 9.8(b) shows the conditional probabilities, $\mathcal{P}(Z_1, \Delta | Z_2, \Delta; \tau_m)$, obtained by dividing the joint probabilities in (a) by the relevant averaged propagators [11]. The shape of the conditional

⁴Note that these are plotted, for convenience, in velocity units rather than displacement units.

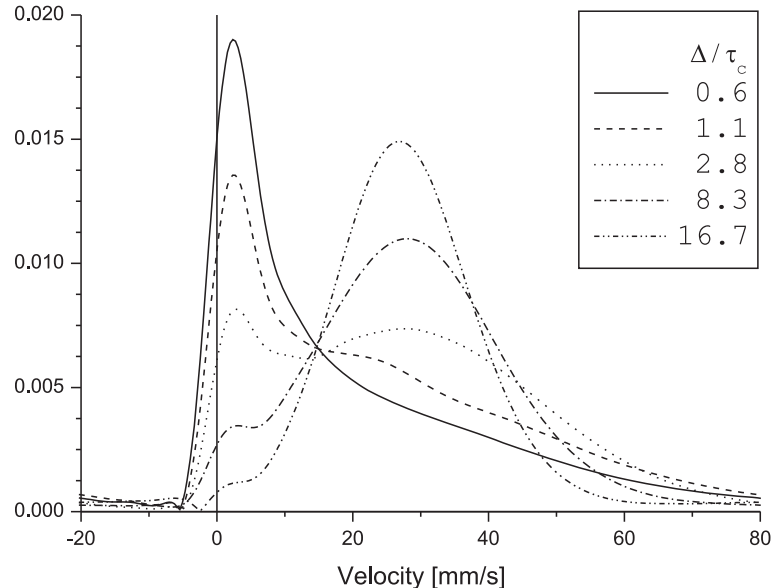


Fig. 9.7 One-dimensional propagators $\bar{P}(Z, \Delta)$ for flow of water in packed beads of 0.5-mm diameter at a volume flow rate of 3.01/h, corresponding to an average velocity of 24 mm s^{-1} . The propagators were obtained with variable encoding times Δ . Note that the displacement is plotted in velocity units, conversion between displacement and velocity being simply made via the encoding time Δ . (Reproduced with permission from Khrapitchev *et al.* [11].)

probability describes the probability of finding a velocity v_2 in the second encoding interval given that a velocity v_1 was observed in the first interval. It can be seen that for the shortest mixing time, a strong correlation exists between v_1 and v_2 . With increasing mixing time, the fluid elements are allowed to sample a wider range of streamlines and the different components of dispersion lead to a loss of memory, so that the conditional probability of v_2 becomes gradually less dependent on the initial value v_1 , the alignment of contour lines changing from the main diagonal toward a flatter slope considerably less than unity.

Of course, the pulse sequence of Fig. 9.5 is idealised. stimulated-echo versions are possible [11], with z -storage during τ_m , as well as sequences in which CPMG trains are inserted to maintain transverse magnetisation during the mixing time, in the latter case, care needing to be taken to sustain both the real and imaginary parts of the signal through the echo train [10]. Note, following our discussion in Chapter 8, the need to use an appropriate phase cycle in order to select the desired magnetisation coherence in the final echo.

Finally, it is worth noting that VEXSY is a pure phase-encoding method and that means that the signal is available with full spectral resolution. That is the upside of a time-costly encoding scheme where separate time steps are needed for each increment of the independent dimensions.

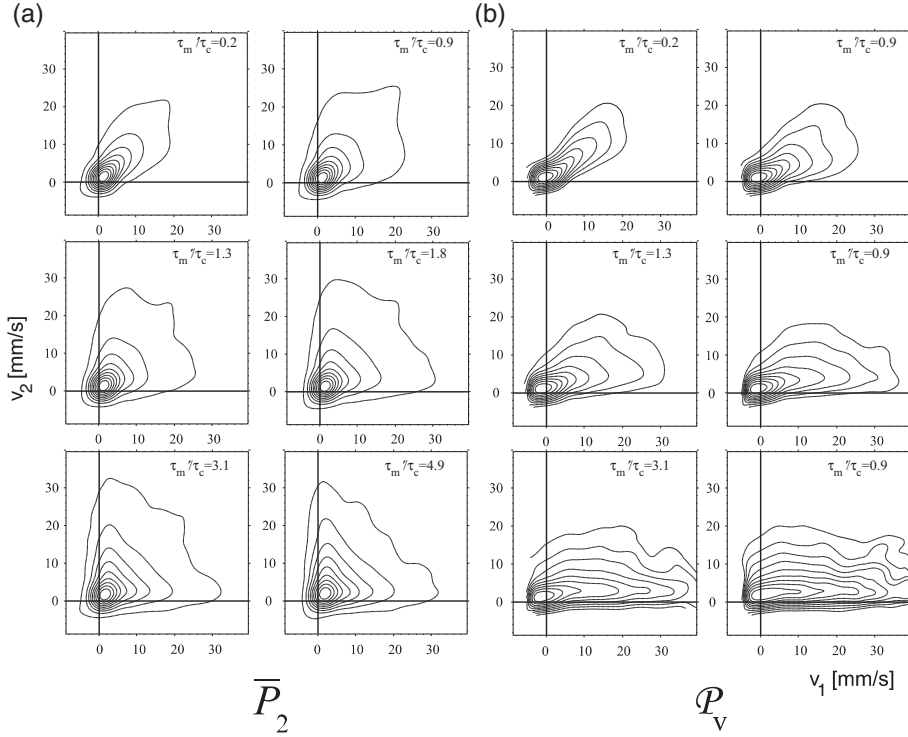


Fig. 9.8 Joint probability density of displacements, $\bar{P}_2(Z_1, \Delta; Z_2, \Delta; \tau_m)$, for water flowing through packed beads of 0.5-mm diameter obtained by the VEXSY experiment, at flow rate of 1.01/l/h, with average velocity $\langle v \rangle$ of 7.9 mm s^{-1} , corresponding to τ_v of 64 ms and $Pe = 1900$. The encoding time is $\Delta = 12$ ms. Velocities measured before and after the mixing interval τ_m are shown along the abscissa and ordinate axes, respectively. Numbers indicate velocities in millimetres per second. Contour lines are in steps of 10% where the peak amplitude is normalised to unity. (b) As in (a), but with the data plotted as the conditional probability $P(\mathbf{R}_1, \Delta | \mathbf{R}_2, \Delta; \tau_m)$. (Reproduced by permission from Khrapitchev *et al.* [11].)

9.3.2 SERPENT

A pulsed gradient spin-echo experiment very similar to VEXSY was proposed by Stapf *et al.* [12], in which three or more sequential gradient pulses are applied to the spin ensemble, each with an arbitrary amplitude, but with the requirement that the time integral of the gradient waveforms over the whole experiment be zero, the condition required for echo formation. This experiment was termed SERPENT, for SEquential Rephasing by Pulsed field gradients Encoding N Time intervals. The comparison of VEXSY and SERPENT is discussed in detail in reference [13]. In the simplest SERPENT manifestation of three successive gradient pulses, the echo constraint determines that two gradient pulses may be independently varied, thus implying a 2-D encoding space. The three-pulse SERPENT and the VEXSY experiments contain precisely the

same information, but with the equivalent mixing time of VEXSY being zero, so that the time interval over which changes in velocity are observed is essentially the velocity encoding time Δ . Because of the flexibility of mixing time setting in the VEXSY experiment, the latter might be more explicitly interpreted as a classic exchange experiment.

9.3.3 POXSY

In a sense, the simplest of all exchange experiments in the Fourier domain of gradient encoding is the positional exchange (POXSY) of Fig. 9.9(a), proposed by Han *et al.* [14]. The pulse sequence has the appearance of a simple Stejskal–Tanner two-

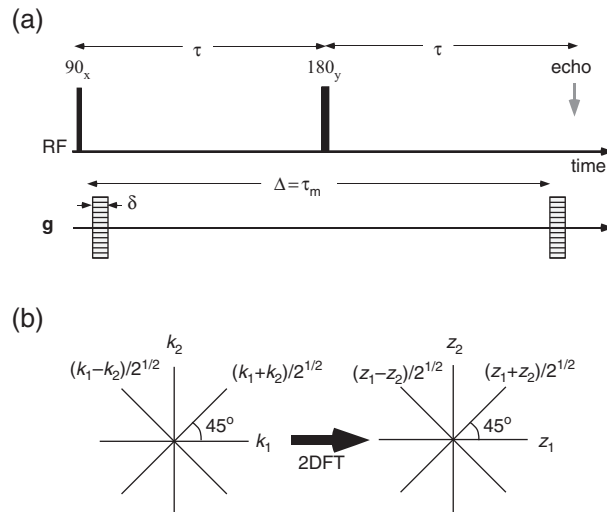


Fig. 9.9 (a) Pulse sequence for positional exchange spectroscopy (POXSY) along with (b) associated axis systems. Note that the diagonal and off-diagonal projections provide access to the mean position and mean displacement, respectively [14].

gradient pulse spin-echo experiment. But rather than having the two gradient pulses stepping in tandem, to ensure the echo condition $\int g^*(t)dt = 0$, two independently varied collinear gradient pulses of wavevector k_1 and k_2 are used to phase encode for position z along the gradient axes. The signal is then

$$S(k_1, k_2, \tau_m) = \iint \rho(z_1) P(z_1|z_2, \tau_m) \exp(ik_1 z_1 + ik_2 z_2) dz_1 dz_2 \quad (9.24)$$

so that 2-D Fourier transformation of $S(k_1, k_2, \tau_m)$ with respect to k_1 and k_2 returns the spectrum $\rho(z_1)P(z_1|z_2, \tau_m)$. This is indeed an exchange experiment in which the mixing time, $\tau_m = \Delta$ and where $\rho(z_1)P(z_1|z_2, \tau_m)$ is the probability that a spin-bearing particle at z_1 at time zero has moved to z_2 after time $\tau_m = \Delta$.

Han *et al.* point out that the diagonal and off-diagonal projections of the 2-D signal and its Fourier spectrum relate simply to the mean position ($z_1 + z_2$) and mean displacement ($z_1 - z_2$), as shown in the conjugate axes of Fig. 9.9(b).

9.3.4 Two-dimensional propagators

An entirely different approach to 2-D PGSE NMR has been taken by Stapf *et al.* [15] using a single effective gradient pair PGSE NMR sequence, but one in which the gradient pulses comprise q_X and q_Z components that are independently stepped, in effect traversing a 2-D Cartesian raster in q -space. Two dimensional Fourier transformation returns a 2-D average propagator $\bar{P}(X, Z, \Delta)$. The method is particularly interesting when applied to dispersive flow, in which Z refers to the flow direction while X is transverse to the flow, leading to intrinsic asymmetry in the distribution. Figure 9.10 shows an example of $\bar{P}(X, Z, \Delta)$ for water flowing at $\langle v \rangle = 2.5 \text{ mm s}^{-1}$ through a pack of 0.6-mm diameter beads [15], for which $\tau_v = 240 \text{ ms}$. Also shown are the projections of this distribution along each of the axes, in effect, the one-dimensional average propagators $\bar{P}(X, \Delta)$ and $\bar{P}(Z, \Delta)$, respectively, where $\Delta \approx \tau_v$. Note the similarity of the propagator $\bar{P}(Z, \Delta)$ to that shown in Fig. 9.7 under similar conditions.

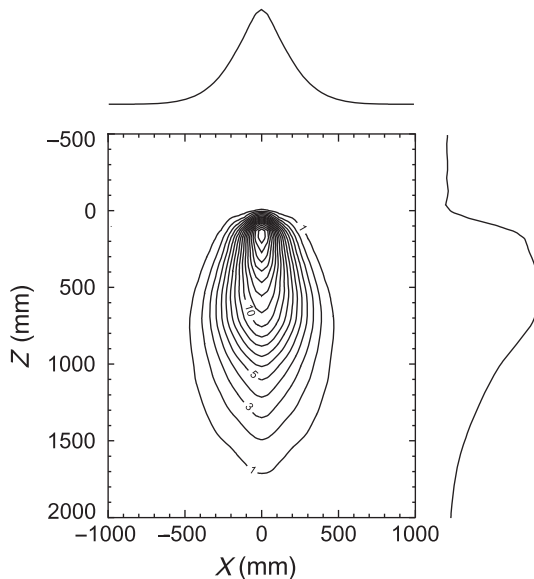


Fig. 9.10 Normalised, experimental 2-D average propagator $\bar{P}(X, Z, \Delta)$ in a 0.6-mm diameter bead pack at a flow rate of 42.0 ml min^{-1} and with $\Delta = 231 \text{ ms}$. The projections, $\bar{P}(X, \Delta)$ and $\bar{P}(Z, \Delta)$, are drawn along the x - and z -axis, respectively. (Reproduced with permission from Stapf *et al.* [15].)

An intriguing aspect of the 2-D average propagator $\bar{P}(X, Z, \Delta)$ is the degree to which it differs from the joint probability formed by simply taking the product of $\bar{P}(X, \Delta)$ and $\bar{P}(Z, \Delta)$. Any difference must arise from correlations within the

flow field. For example, the difference is zero if displacements X and Z are mutually independent, the case for Brownian motion in an isotropic system. Figure 9.11 shows both $\bar{P}(X, Z, \Delta)$ and $\bar{P}(X, Z, \Delta) - \bar{P}(X, \Delta)\bar{P}(Z, \Delta)$ for a range of Péclet numbers. The difference terms, which integrate to zero because of the normalisation employed, show quite remarkable positive and negative structure, clearly indicating the role of subtle correlations in the flow. However, the interpretation of these correlations is problematic, the authors quoting the statisticians' perspective [16] that 'the mathematical representation of the relationship, once demonstrated, is an art in itself.'

A more fundamental measure of flow correlations is perhaps given by the non-local dispersion tensor, the measurement of which was demonstrated in Chapter 8. For this tensor, arguably richer in detailed structure than the correlation distributions of Fig. 9.11(b), the statistical physics is explicit, and the patterns derived possibly more intuitive in their connection with the complexities of the flow field.

9.3.5 Inhomogeneous field exchange

Perhaps the simplest possible 2-D Fourier exchange method relevant to diffusion or flow in porous materials utilises spin phase shifts that arise from precession in the inhomogeneous local fields [17], rather than as a result of applied magnetic field gradients. Utilising the distribution of Larmor frequencies resulting from susceptibility inhomogeneity, such a 2-D exchange technique can be used to investigate molecular motion through a porous medium.

As imbibed liquid molecules diffuse through the inhomogeneous magnetic field of the pore space, they migrate between regions of different Larmor frequency, thus causing a broadening in the off-diagonal width of the 2-D spectra. As the mixing time is increased, the mean diffusion distance increases, resulting in an increasing off-diagonal intensity.

The pulse sequence used and shown in Fig. 9.12(a) is similar to a NOESY (Nuclear Overhauser Exchange SpectroscopY) [19], with a frequency encoding (t_1) and acquisition time (t_2) separated by a mixing time, τ_m . The method has been demonstrated with a bead pack comprising 100-micron diameter glass spheres saturated with water. At a proton Larmor frequency of 400 MHz, the resulting inhomogeneous linewidth was 5.2 kHz (FWHM). Using 256 data points at 20 kHz acquisition and evolution bandwidths, the longest evolution time is thus 12.8 ms, corresponding to a diffusion length of around 7 microns, much smaller than the pore dimensions, so that it is possible to approximate the pulse sequence of Fig. 9.12(a), resulting in an approximately 'instantaneous' frequency encoding so that all molecular motion may be considered to occur over the mixing period, τ_m . Clearly for such experiments, large linewidths or large length scales are advantageous in underpinning this assumption. These results are shown in Fig. 9.13, where each 2-D spectrum has been normalised to constant total intensity so as to remove T_1 relaxation effects. A clear growth of off-diagonal intensity is observed as the mixing time is increased. The line broadening can be quantified by taking an average of two intensities located at equidistant points in the off-diagonal direction from the centre peak, and a plot of intensity versus τ_m can be used to estimate the characteristic exchange time for molecular migration across pores.

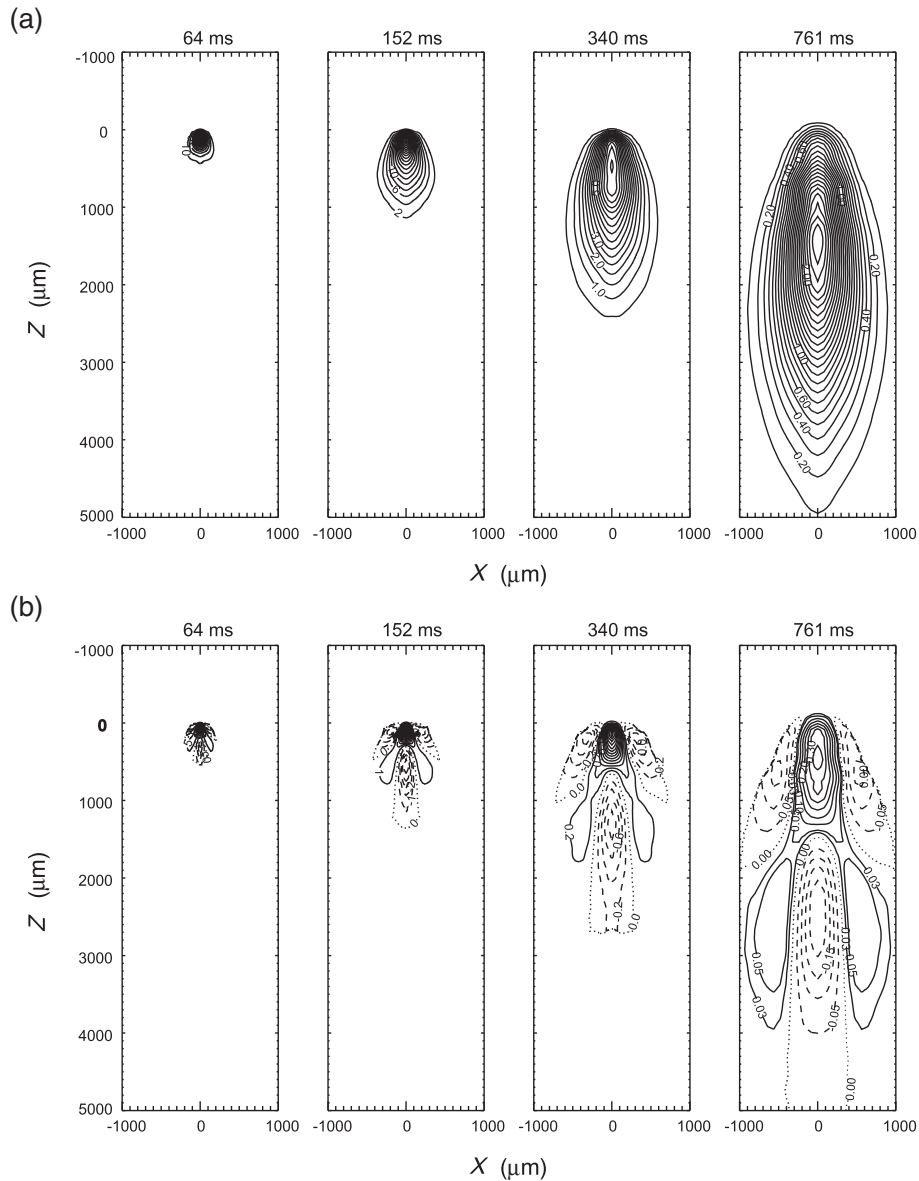


Fig. 9.11 (a) Normalised, experimental 2-D average propagator $\bar{P}(X, Z, \Delta)$ in a 0.6-mm diameter bead pack at a flow rate of 42.0 ml min^{-1} . Evolution times Δ are as indicated. (b) Corresponding difference propagator $\bar{P}(X, Z, \Delta) - \bar{P}(X, \Delta)\bar{P}(Z, \Delta)$. Positive values are indicated by solid lines and negative values by dashed lines. (Reproduced with permission from Stapf *et al.* [15].)

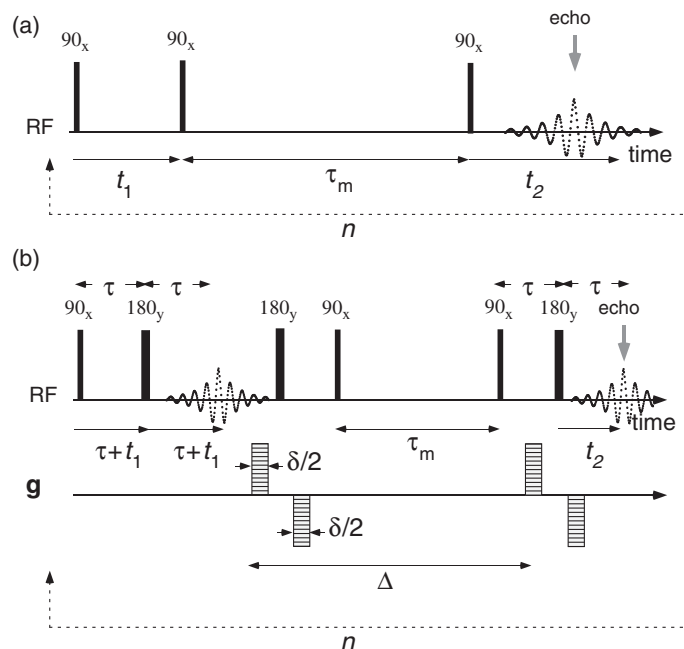


Fig. 9.12 (a) 2-D pulse sequence used for a local field exchange experiment. The evolution time, t_1 , is incremented for each n . The mixing time, τ_m , is kept constant for each repetition, but varies for each experiment. (Adapted from reference [17].) (b) Sequence used for a propagator-resolved version of the local field exchange experiment in which both t_1 and the field gradient pulse amplitude g are independently stepped. Note the use of bipolar gradients to reduce susceptibility artifacts in the propagator dimension. (Adapted from reference [18].)

Propagator-resolved inhomogeneous field exchange

The inhomogeneous local field exchange experiment may be extended [18] to include a third Fourier space, as shown in Fig. 9.12(a), where independently stepped gradient pulses allow for a propagator dimension. By this means one may distinguish molecules that have diffused different distances along the field gradient axis. Hence, rather than measuring an off-diagonal intensity that is a function of mixing time alone, the additional spatial dimension allows a spatio-temporal analysis of the diffusion between sites of differing field.

9.4 Fourier–Laplace methods

In a pioneering 1981 paper, Stilbs suggested [20] that the molecular self-diffusion coefficient could be used to separate high-resolution NMR spectra according to molecular size, an effect he termed ‘size-resolved NMR’. With the practical realisation of this idea through the advent of new data processing techniques, this method has come to be known as DOSY (for Diffusion Ordered SpectroscopY)—a term coined by Morris and Johnson [21]—or, in another variant, CORE-NMR (for COnponent REsolved NMR spectroscopy) [22]. From a broad perspective, these 2-D methods maintain the

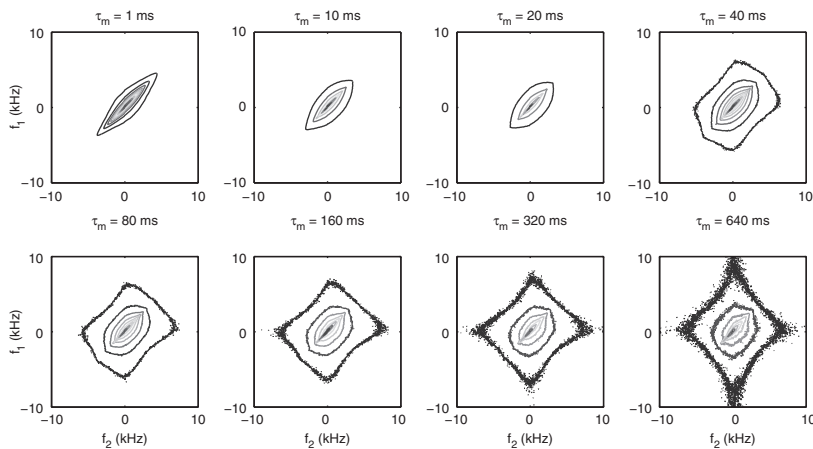


Fig. 9.13 2-D ^1H NMR exchange spectra obtained from water in 100-micron diameter bead pack at 400 MHz with a 20 kHz bandwidth. The eight examples show mixing times ranging from 1 to 640 ms. In each case the T_1 relaxation that occurs over the mixing time is compensated by normalising the total intensity in the spectrum, leading to noisier spectra at large τ_m . (Reproduced with permission from reference [17].)

full high resolution NMR spectrum as dimension in a Fourier domain, while distributing these spectra by diffusion coefficient in an inverse Laplace domain. They are not the only examples of possible 2-D Fourier–Laplace spectroscopies. Clearly one might correlate NMR spectra and relaxation rates, though the latter are more often chemical site-specific rather than molecule-specific, and hence do not present quite the same ‘molecular separation’ utility as CORE or DOSY. In the physics of porous media, the relaxation time may often be used as a marker for pore size, so that the Fourier–Laplace planes of inhomogeneous field- T_2 or displacement propagator- T_2 can provide useful insights. In this section we present examples of such 2-D Fourier–Laplace variants.

9.4.1 Diffusion-resolved spectroscopy

One simple approach to diffusion-resolved spectroscopy was demonstrated by Morris and Johnson [21]. Using the stimulated-echo PGSE NMR sequence shown in Fig. 9.14, they generated a 2-D data set by stepping the gradient amplitude in the first dimension and acquiring the free induction decay in the second. In order to ensure that eddy current effects from the gradient pulse switching had decayed before spectral sampling, they stored the stimulated echo along the z -axis for a sufficient period τ_e (around 10 ms) before recall and acquisition, a method referred to as longitudinal eddy current decay (LED) [23]. During τ_e homospoil, gradient pulses may be used to remove unwanted signals from the acquisition period.

The signal, normalised to the zero gradient case $q = 0$, could be written in continuous form as

$$S(t, q) = \iint \exp(-i\omega t) \exp(-q^2 D \Delta) f(\omega, D) d\omega dD \quad (9.25)$$

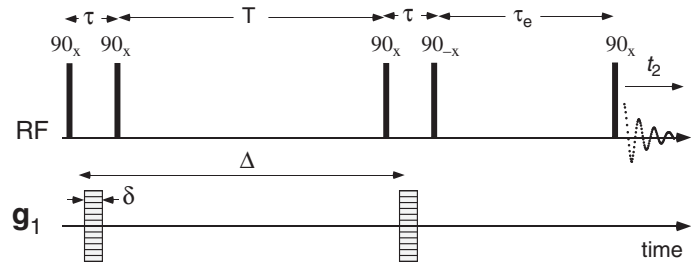


Fig. 9.14 2-D diffusion-ordered spectroscopy sequence of Morris and Johnson [21], in which a stimulated-echo sequence is employed with the gradients stepped to provide the first (inverse Laplace) dimension and the signal acquired in time in the second (Fourier) spectral dimension. The magnetisation arising at the echo after the third 90° RF pulse is stored along the z -axis for later recall, to allow all eddy current effects from the last gradient pulse to decay before recall of the signal for spectral analysis.

and, where necessary, with Δ replaced by $\Delta - \delta/3$ to allow for finite gradient pulse-width effects. Discretely encoded, we would represent these integrals by

$$S(t_i, q_j^2) = \sum_{k=1}^{M_1} \sum_{l=1}^{M_2} \exp(-i\omega_k t_i) \exp(-q_j^2 D_l \Delta) f(\omega_k, D_l) + \epsilon_{i,j} \quad (9.26)$$

where t_i ($i = 1..N_1$) are the sampling times of the acquisition dimension t_2 , and q_j^2 ($j = 1..N_2$) are the squared-wavevectors of the evolution dimension associated with gradient stepping. An *a priori* domain of discrete frequencies ω_k and diffusion coefficients D_l is implied, the former being the usual Fourier domain of the NMR signal acquisition from which the spectrum arises. The second domain requires inverse Laplace transformation to reveal the diffusion coefficient distribution.

Morris and Johnson carried out this inversion both using regularised 1-D NNLS (CONTIN [6]) and by a programme that fitted to a predefined maximum number of exponential decays. To the extent that a known number, N , of molecular species is present in the sample, eqn 9.27 can be rewritten

$$S(t_i, q_j^2) = \sum_{n=1}^N \sum_{k=1}^{M_1} A_n(\omega_k) \exp(-i\omega_k t_i) \exp(-q_j^2 \Delta D_n) + \epsilon_{i,j} \quad (9.27)$$

where $A_n(\omega_k)$ is the concentration-weighted NMR spectrum of the n th molecule. Of course the prior knowledge that each molecule has a unique diffusion coefficient argues against the use of a regularised NNLS inversion procedure in which broad diffusion distributions are favoured. Furthermore, in a large time-domain data set, perhaps 16k or 32k in size, the number of 1-D NNLS inversions to be performed is particularly large and therefore time-consuming. Where the number of molecular components is known, the use of simple multi-exponential fitting with a predetermined number of components is not only less time-consuming, but also produces a more physically realistic discrete diffusion spectrum. A powerful approach to inverting the q^2 -domain data has been proposed by Stilbs *et al.* [22]. Their CORE-NMR uses a global procedure in which the

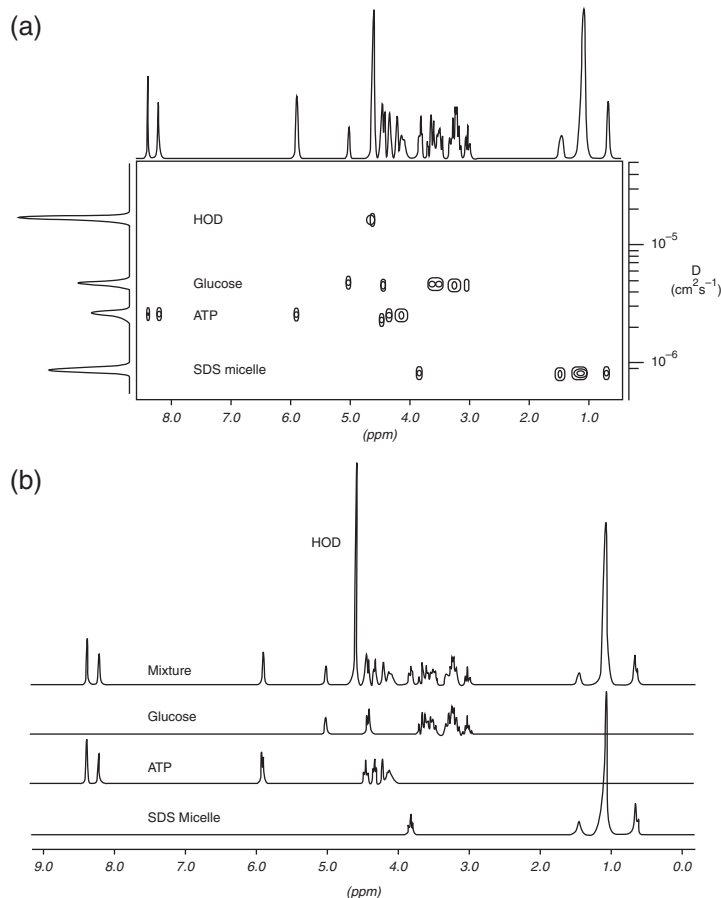


Fig. 9.15 Illustration of diffusion-ordered NMR: (a) 2-D frequency-diffusion coefficient spectrum for a mixture containing D_2O , glucose, ATP, and SDS micelles; (b) individual spectra of components in the mixture obtained by projection of intensities in the various diffusion ranges onto the chemical shift axis. (Reproduced with permission from Morris and Johnson [21].)

entire 2-D data set is fitted utilising the intrinsic common diffusive echo attenuations of individual components in the phased, absorption-mode spectra, the only fitting parameters in addition to the N diffusion coefficients being the N amplitudes for the contribution of each component. The method is efficient and ideally suited to large spectral data sets. The CORE approach relies on the ‘prior knowledge’ that a component bandshape (i.e. all frequencies) identically follow the same PGSE decay pattern, thus stabilising the processing and enhancing the signal-to-noise ratio.

9.4.2 Propagator-resolved T_2

Britton *et al.* [24] have used Fourier–Laplace spectroscopy to correlate relaxation times with molecular translational displacements in the case of water flowing through a packed bed of porous hydrogel particles ranging from 1 mm to 3 mm in diameter.

Their pulse sequence, shown in Fig. 9.16, incorporates a stimulated echo as the PGSE segment, with z -storage of magnetisation for later recall to a CPMG echo train of echo spacing τ_E . In order to accurately represent the propagators for displacement following Fourier transform with respect to q , a full complex signal must be acquired, necessitating storage of both x - and y -components of magnetisation during the PGSE segment, with appropriate recall and CPMG refocusing of both components through the remainder of the sequence. In consequence, the chosen phase cycle must reflect these requirements.

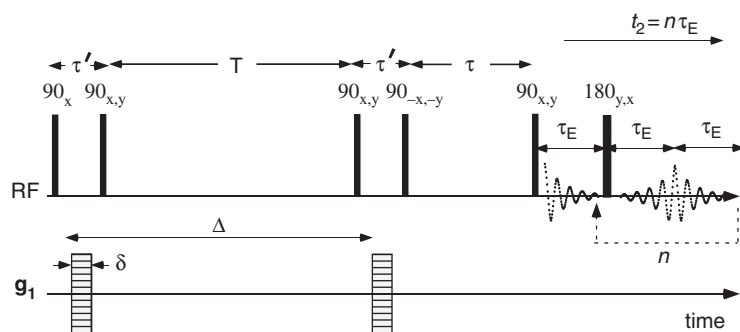


Fig. 9.16 RF and gradient pulse sequences for a T_2 -resolved propagator experiment, comprising a pulsed gradient stimulated echo experiment followed by a CPMG train. As for the LED sequence, magnetisation is stored along the z -axis for later recall. Note that the phase cycle must store both x - and y -components of the magnetisation for correct reconstruction of the propagator.

The particles were formed by spraying droplets of alginate solution into 0.1 M calcium chloride. Water T_1 relaxation times and self-diffusion coefficients were the same inside the gel beads and in the outside pore fluid, at 1.8 s and $2 \times 10^{-9} \text{ m}^2 \text{s}^{-1}$, respectively, at 293 K, suggesting an open unrestricted gel structure. T_2 values are, however, widely distributed, in approximately three groups: short ($T_2 < 30 \text{ ms}$), intermediate ($T_2 \sim 300 \text{ ms}$), and long ($T_2 > 1 \text{ s}$). These groups had been tentatively identified in an earlier T_2 -only study [25] as water inside the beads and, for the medium and long T_2 values, as water in the pores between beads. Once flow is initiated, the propagator enables one to clearly recognise water resident within beads, water exchanging between the bead and the pore space, and water freely flowing along the interconnected pore space. Figure 9.17 shows the 2-D propagators that result from Fourier transformation with respect to q to produce a propagator for each echo in the CPMG train, followed by 1-D inverse Laplace transformation of the CPMG decays for each point (Z) in the propagator, by means of CONTIN.

The correlation apparent in Fig. 9.17 is quite powerful. The longest and shortest relaxation components are respectively associated with fluid remaining predominantly in the pore (the largest fluid displacements) and bead (the least fluid displacement). The finite displacement associated with the intermediate T_2 peak is consistent with

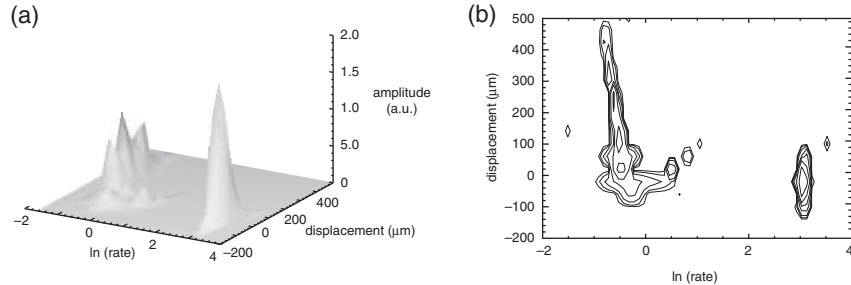


Fig. 9.17 (a) Surface and (b) contour plots of the T_2 -resolved propagators, $\bar{P}(Z, \Delta, T_2)$, for water flowing through 3-mm diameter beads at an average flow velocity of 0.5 mm s^{-1} . (Reproduced with permission from Britton *et al.* [24].)

exchange between the beads and the pore space. This example is instructive. Where a 1-D experiment provides the opportunity to reasonably speculate, such a 2-D correlation experiment allows a much more confident interpretation, one which enables the subsequent use of efficient 1-D techniques with greater information content.

9.5 Multidimensional Laplace–Laplace correlation methods

The idea that one could perform a 2-D NMR experiment in which Laplace inversions are performed in each dimension goes back to a relaxation exchange experiment proposed by Lee *et al.* in 1993 [26], in which independent 1-D transformations were applied to each dimension in succession, with the consequential disadvantages discussed in Section 9.2.3. The first integrated 2-D Laplace–Laplace NMR experiments were the $T_1 - T_2$ and $T_2 - D$ correlations carried out by Song, Hürlimann, and co-workers [27–29]. 2-D exchange measurements followed [30], and soon a plethora of possible dimensions were demonstrated, involving relaxation rates, diffusion coefficients, and internal magnetic field gradients.

Our summary begins with correlation methods. In each case these involve two or more encodings in sufficiently quick succession that the parameters to be extracted by ILT in each dimension correspond to molecular-borne spins at ‘the same time’. Ideally, such encodings would be simultaneous and of infinitesimal duration. In practice, they will always require finite time, and almost invariably follow in succession. In consequence, interpretation of the measurements as true correlations requires prior knowledge that molecular behaviours are indeed consistent over the total encoding time.

9.5.1 Relaxation–relaxation

A $T_1 - T_2$ correlation pulse sequence is shown in Fig. 9.18 in which there is an evolution time, t_1 , associated with spin-lattice relaxation, and a multi-echo acquisition time, t_2 , associated with spin spin relaxation, where t_2 relates to echo maxima at time positions $t_2 = n\tau_E$. Assuming continuous time and relaxation-rate variables, and continuous relaxation-spectrum density, $f(R_1, R_2)$, we would write the signal, normalised to its value at $t_1 = t_2 = 0$, as

$$S(t_1, t_2) = \iint (1 - 2 \exp(-R_1 t_1)) \exp(-R_2 t_2) f(R_1, R_2) dR_1 dR_2 \quad (9.28)$$

where R_1 and R_2 refer to the relaxation rates T_1^{-1} and T_2^{-1} . Again, to make clear the discrete form,⁵ and using explicit discretisation of the two independent encoding times, the signal can be written

$$S(t_{1i}, t_{2j}) = \sum_{k=1}^{M_1} \sum_{l=1}^{M_2} (1 - 2 \exp(-R_{1k} t_{1i})) \exp(-R_{2l} t_{2j}) f(R_{1k}, R_{2l}) + \epsilon_{i,j} \quad (9.29)$$

Note that the use of an inversion recovery stage implies that the kernel in the Fredholm integral problem, $(1 - 2 \exp(-R_1 t_1)) \exp(-R_2 t_2)$, can have both positive and negative sign. The principles outlined in Section 9.2 remain the same, however. A more subtle issue concerns our assumptions regarding the sign of $f(R_1, R_2)$. The numerical ILT assumes positive amplitudes for $f(R_1, R_2)$. As we will see, there are circumstances in which they may be negative. For the moment, however, we will discuss an example where this problem does not arise.

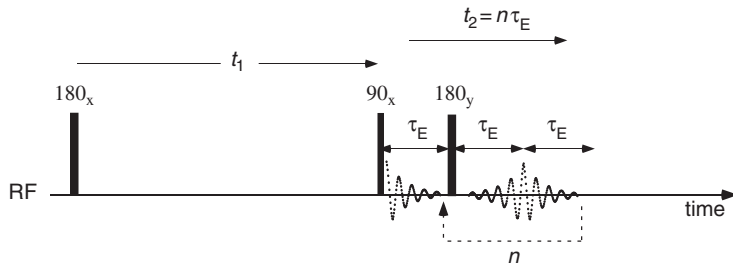


Fig. 9.18 RF pulse sequences for a $T_1 - T_2$ correlation experiment comprising an inversion-recovery segment followed by a CPMG train.

Figure 9.19 gives an example of the results of an experiment carried out on a sedimentary (limestone) rock sample saturated with brine, in which the distribution of pore sizes covers a wide range, and the T_1 and T_2 distributions are broad [27]. The time-domain data comprised 30 values of t_1 ($N_1 = 3$) and 4096 T_2 points ($N_2 = 4096$), where t_1 was varied logarithmically from $10\ \mu\text{s}$ to a few seconds, while the values of T_2 were equally spaced with a step size of $200\ \mu\text{s}$. Sixty-four scans were accumulated, at 5 s repetition time, to improve the signal-to-noise ratio, with the total experiment lasting 2.7 h. The size of the matrix in the Laplace domain ($M_1 \times M_2$) was 100×100 . The $T_1 - T_2$ spectrum reveals two separate peaks and a shoulder at $T_2 \approx 20\ \text{ms}$. The major peak at long T_1 and T_2 approaches the line of $T_1 = T_2$ expected for bulk water. By contrast the peak at shorter relaxation times is close to the line $T_1 = 4T_2$, typical for water in pores, where surface relaxation effects dominate. The behaviour

⁵From now on we shall use a continuous representation only, the discretisation process being apparent.

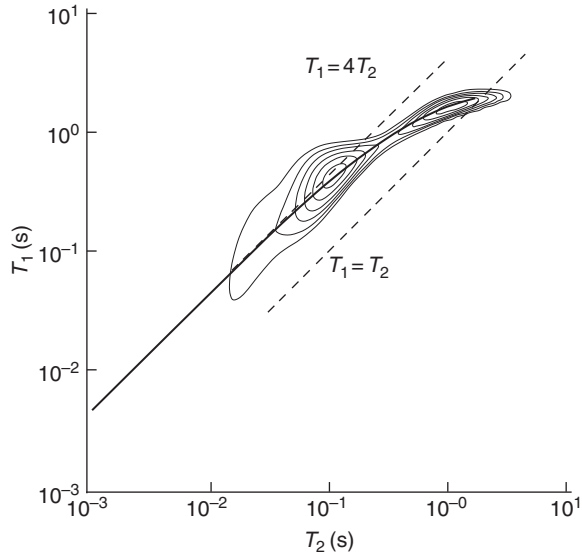


Fig. 9.19 Contour plots of $T_1 - T_2$ correlation spectrum for water in limestone. The dashed lines are for $T_1 = T_2$ and $T_1 = 4T_2$. The solid thick line is the theoretical behaviour of the sum of surface and bulk contributions to T_1 and T_2 . (Reproduced with permission from Song *et al.* [27].)

is consistent with the rock structure indicated from optical microscopy, where grains containing small pores are close-packed with large inter-grain void spaces of around $100\text{ }\mu\text{m}$ in size. The solid line in Fig. 9.19 is obtained from a simple model in which the relaxation rate is assumed to be a sum of surface and bulk rates, under the condition that the ratio of the surface T_1 and T_2 relaxation times is 4.5.

9.5.2 Negative peaks and coupled eigenmodes

The T_1-T_2 correlation experiment is intriguing in the case of porous media where surface relaxation effects determine both relaxation modes. Under special circumstances, negative off-diagonal peaks may appear in the spectrum [31, 32]. Clearly the numerical inverse Laplace method cannot reveal such peaks and so great care is needed in this case.

The argument is simply followed using the normal modes description of the Brownstein–Tarr relaxation model, as described in Section 6.3.2 Chapter 6, starting with the magnetisation eqn 6.38 rewritten in terms of the pulse sequence of Fig. 9.18 (as [32]):

$$M(\mathbf{r}, t_1) = \sum_{p=0}^{\infty} a_p u_{1,p}(\mathbf{r}) \exp(-t_1/T_{1,p}) \quad (9.30)$$

and

$$M(\mathbf{r}, t_1, t_2) = \sum_{q=0}^{\infty} b_q u_{2,p}(\mathbf{r}) \exp(-t_2/T_{2,q}) \quad (9.31)$$

where the 1 and 2 subscripts refer to T_1 and T_2 , respectively, and where $b_q = \int u_{2,q}^*(\mathbf{r})M(\mathbf{r}, t_1)d\mathbf{r}$. Separate normal modes may be assigned to T_1 and T_2 relaxation because of their differing boundary conditions, i.e.,

$$D\hat{\mathbf{n}} \cdot \nabla u_{1,n}(\mathbf{r}) + \bar{\rho}_1 u_{1,n}(\mathbf{r})|_S = 0 \quad (9.32)$$

and

$$D\hat{\mathbf{n}} \cdot \nabla u_{2,n}(\mathbf{r}) + \bar{\rho}_2 u_{2,n}(\mathbf{r})|_S = 0 \quad (9.33)$$

Of course $M(\mathbf{r}, t_1, t_2)$ is the measured 2-D signal and ideal inverse Laplace transformation therefore leads to a 2-D spectrum $S(T_1, T_2)$ where each relaxation mode $\exp(-t/T_n)$ is replaced by $\delta(T - T_n)$. Song *et al.* [32] have pointed out that off-diagonal peaks in the T_1-T_2 spectrum indicate the degree of non-orthogonality of $u_{1,n}$ and $u_{2,n}$, since

$$S(T_1, T_2) = \sum_{p,q} \langle f | u_{2,q} \rangle \langle u_{2,q} | u_{1,p} \rangle \langle u_{1,p} | i \rangle \delta(T_1 - T_{1,p}) \delta(T_2 - T_{2,q}) \quad (9.34)$$

where the shorthand $\langle \phi | \varphi \rangle$ represents $\int \phi^*(\mathbf{r})\varphi(\mathbf{r})d\mathbf{r}$, $\langle u_{1,p} | i \rangle = a_p$, $|i\rangle$ being the initial magnetisation distribution, $M(\mathbf{r}, 0)$. Similarly $|f\rangle$ is the final magnetisation distribution and can be assumed uniform for the purpose of calculation.

Song *et al.* [32] have pointed out that off-diagonal peaks in the T_1-T_2 spectrum indicate the degree of non-orthogonality of $u_{1,n}$ and $u_{2,n}$, as expressed in $\langle u_{2,q} | u_{1,p} \rangle$. For example, if the T_1 and T_2 surface relaxivities are identical, then so are the modes, and orthogonality ensures $\langle u_{2,q} | u_{1,p} \rangle = 0$, so that no off-diagonal contributions appear. Similarly, if both T_2 and T_1 are in a fast diffusion limit, i.e. $\bar{\rho}_{1,2}a/D \ll 1$, the T_2 and T_1 are in a common zeroth-order mode, u_0 , and no off-diagonal features will be apparent. However, these authors have shown that in the intermediate case $\bar{\rho}_{1,2}a/D \sim 1$, clear off-diagonal structure is apparent and, remarkably, that those off-diagonal peaks are antisymmetric [31], with negative peaks seen in the ‘non-physical’ region of the spectrum where $T_2 > T_1$. Song *et al.* [32] have also demonstrated the existence of negative off-diagonal T_1-T_2 peaks in the case where spins diffuse from pore to pore.

Clearly the matter of negative peaks is problematic. Numerical inverse Laplace transformations are based on an amplitude positivity constraint, and so such peaks will not only be invisible, but their presence may distort the apparent spectrum. Ideally, they should not appear in $T_1 - T_1$ or $T_2 - T_2$ exchange experiments (discussed in Section 9.6), where the modes are orthogonal, resulting in off-diagonal peaks that are positive and symmetric. However, relaxation during the intervening mixing time has the potential to mix modes, thus making negative off-diagonal peaks possible [33]. The problem may be less likely in other correlation experiments, such as $D - T_2$, where quite independent physics governs the different relaxation parameters. Nonetheless, where a physical model is proposed in order to generate a 2-D spectrum, it should be tested for amplitude sign prediction in the manner outlined above.

9.5.3 Diffusion–relaxation

The diffusion T_2 relaxation correlation experiment can be performed using exactly the same sequence shown in Fig. 9.16 for the propagator- T_2 experiment of Section 9.4.2. The only difference is that the relevant gradient-pulse-induced kernel is that for diffusion, with the 2-D ILT being used to generate the $D-T_2$ spectrum. Rewriting eqn 9.20 using the explicit Stejskal–Tanner expression involving the gradient amplitude g_1 , we have the signal (normalised to $g_1 = 0$)

$$S(g_1, t_2) = \iint \exp(-\gamma^2 g_1^2 \delta^2 D(\Delta - \delta/3)) \exp(-t_2 R_2) f(D, R_2) dD dR_2 \quad (9.35)$$

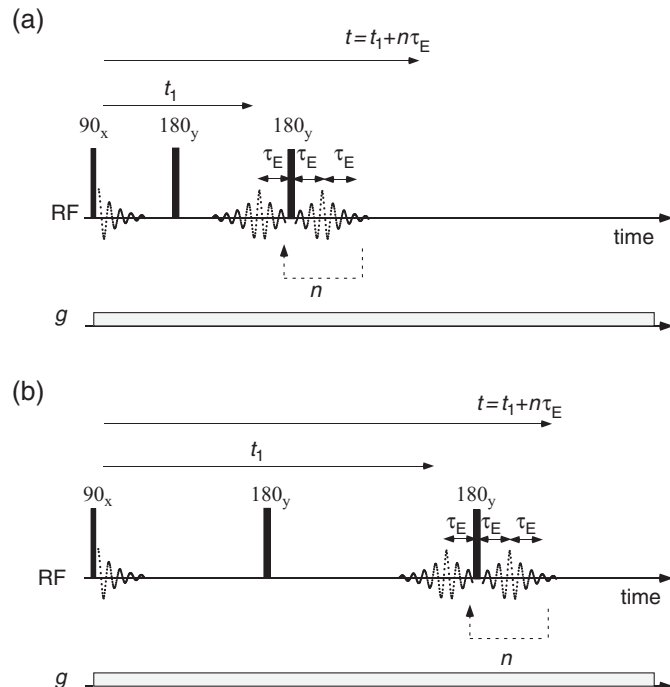


Fig. 9.20 Pulse sequence used to acquire diffusion-relaxation data in inhomogeneous fields. After the initial nominal 90° pulse, a series of echoes are generated with 180° pulses. The first two echo spacings, $t_1/2$, are longer than the later echo spacings, τ_E , such that the first echo amplitude is sensitive to diffusion while the echo train is sensitive only to T_2 , because τ_E is so short. (a) and (b) show repeats, with different values of t_1 and the other independent time variable, $t = t_1 + n\tau_E$. [34].

Of course there are other means by which $f(D, R_2)$ may be measured. In particular, the diffusion-encoding can be performed using steady gradients and variable diffusion times, especially convenient in ‘down bore hole’ applications where pulsed gradient capabilities may be absent. Figure 9.20 shows just such a sequence [28] employed to take advantage of a constant background gradient, g . For down bore hole applications,

the pulse sequence shown in Fig. 9.20 can be made more robust with respect to motion effects by using two initial echoes rather than a single echo [28].

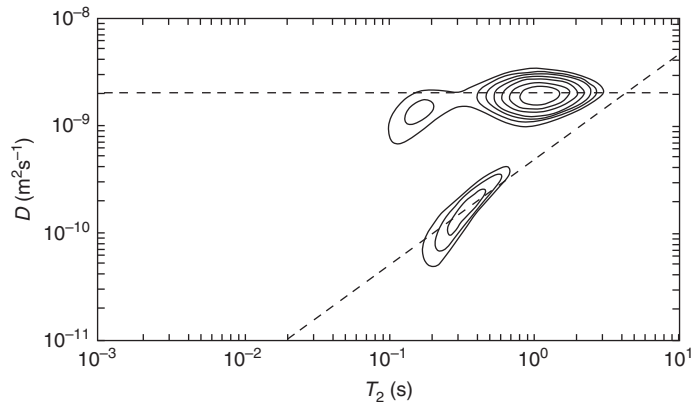


Fig. 9.21 Diffusion-relaxation correlation maps for a dolomite sample saturated with water and oil. The contour lines are at multiples of 12.5% of the maximum value in each graph. (Reproduced with permission from Hürlimann *et al.* [34].)

For such a sequence, the signal is given by

$$S(t_1, t) = \iint \exp\left(-\frac{1}{12}\gamma^2 g^2 D_k t_1^3\right) \exp(-tR_2) f(D, R_2) dD dR_2 \quad (9.36)$$

Figure 9.21 shows the $f(D, R_2)$ distribution for a sample of Dolomite containing both water and oil. The horizontal dashed line indicates the diffusion coefficient of free water, while the sloping dashed line corresponds to the relaxation-diffusion correlation data for alkanes [35].

It is important to note that, for simple pore structures, where restricted diffusion and surface relaxation effects for imbibed fluid molecules play an important role in determining the NMR spin-echo signal behaviour, the dependence of the echo amplitude on gradient pulse strength will be complex because of q -space diffraction effects, and the decay of the echo amplitude with time will be multi-exponential because of the Brownstein–Tarr modes. Consequently, $D - T_2$ plots obtained from simple encoding sequences, such as that shown in Fig. 9.16, can lead to a quite complex response on 2-D inverse Laplace transformation [36]. An example of such a 2-D map calculated for spherical pores is shown in Fig. 9.22, over a wide range of diffusive observation times Δ and surface relaxivities $\bar{\rho} = M$, where these are expressed in appropriate dimensionless units relating to the spherical pore diameter a and the molecular self-diffusion coefficient D_0 . In these plots there exists a dominant primary relaxation-diffusion mode, marked with a diagonal arrow. In order to more clearly reveal the weaker amplitude modes in these 2-D inverse Laplace plots, the analysis was carried out using a lower cutoff value for qa . The choice of cutoff only affects the relative amplitudes of the modes, but not their corresponding $D - T_2$ coordinates.

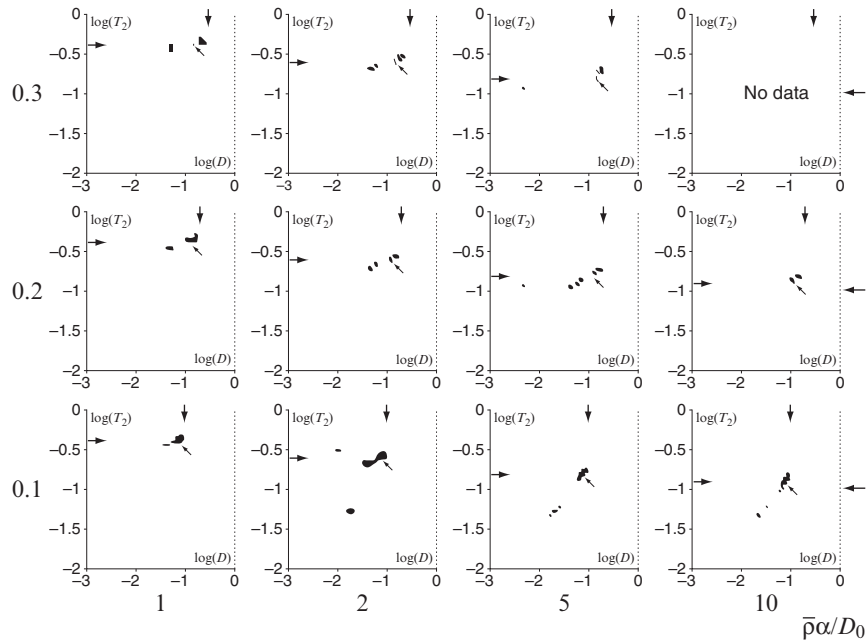
$D_0\Delta/\alpha^2$


Fig. 9.22 2-D $D-T_2$ maps for spherical pores, as a function of $\bar{\rho}a/D_0$ and $D_0\Delta/a^2$. D values are expressed in units of a^2/Δ and T_2 values in units of a^2/D_0 . These maps were obtained by suppressing the amplitude of the primary relaxation-diffusion mode by using a lower cutoff for the q value. The diagonal arrow indicates the position of the primary relaxation-diffusion mode obtained from the low- q data. The vertical arrow indicates D_0 , while the horizontal arrows on the left indicate the positions of the primary relaxation modes $T_2 = a^2/D_0\xi_0^2$. Horizontal arrows on the right indicate the Brownstein–Tarr limit for $\bar{\rho}a/D_0 \gg 1$ of $T_2 = a^2/D_0\pi^2$. (Reproduced with permission from reference [36].)

9.5.4 Diffusion-local field and relaxation-local field

As molecules diffuse in the local internal magnetic field gradients associated with field inhomogeneity, there is a dephasing akin to that experienced by spins in a steady applied magnetic field gradient. In a multispin-echo CPMG sequence, the sensitivity to that dephasing will be determined by the duration of the inter-echo period, the shorter the duration, the less the echo attenuation, according to the principles laid out in Chapter 5. Hence, it is possible to design a pulse sequence that has one of the encoding dimensions sensitive to this effect. Multi-dimensional examples incorporating local gradient dephasing include T_2 -local field [37], T_1 -local field [38], diffusion-local field [39], and a 3-D example incorporating diffusion, local field, and relaxation [39, 40].

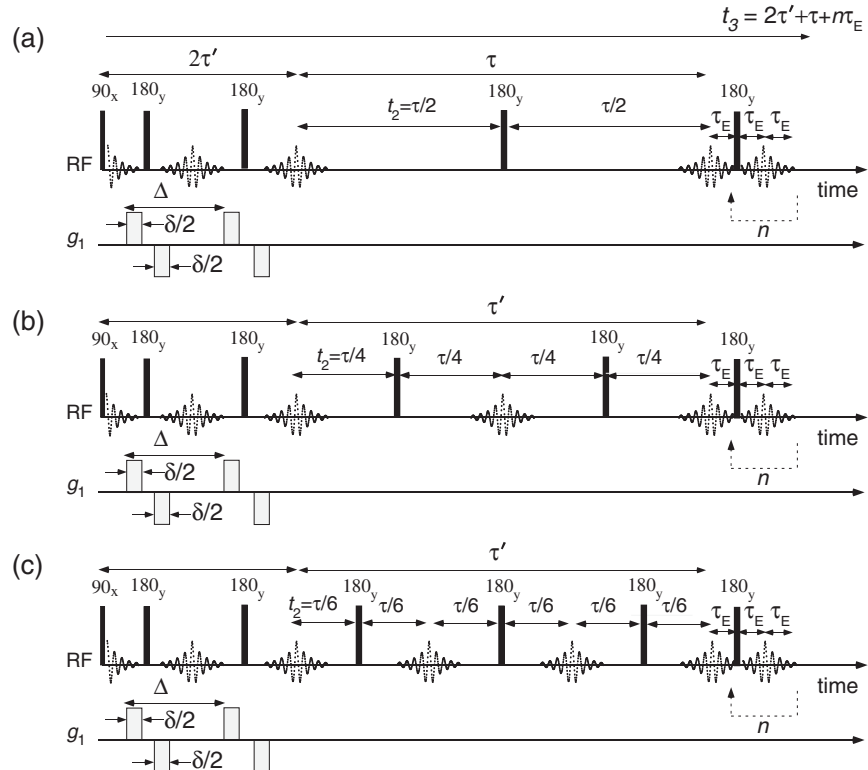


Fig. 9.23 3-D pulse sequence for measurement of correlations between diffusivity, internal gradients, and transverse relaxation. [37, 39]. Three segments operate. In the first dimension the pulsed gradient g_1 is stepped (note the use of a 13-interval sequence to reduce the effect of background gradients), in the second (t_2 dimension), over a fixed time τ , the numbers of 180° RF pulses is stepped—see (a) to (b) to (c)—thus changing the sensitivity of the sequence to diffusion in internal gradients. Finally the numbers of 180° RF pulses at fixed separation interval, τ_E , is incremented to provide the t_3 dimension sensitive to transverse relaxation.

For efficiency, we show a pulse sequence for such 3-D encoding in Fig. 9.23. Any 2-D subset of that sequence can be derived by eliminating the unwanted encoding element. Sequentially, the pulse train begins with a bipolar PGSE encoding (dimension g_1) designed to be sensitive to diffusion. Next comes a constant interval of time (τ) over which the number of 180° RF pulses in a CPMG train is varied so that the variable (second dimension) echo spacing interval becomes $t_2 = \tau/2n$, where n is an integer. As one increases the number of pulses in the fixed time period τ , the spin-bearing molecules have less time to diffuse through the internal gradients, lessening the dephasing effect. Below some value of n , the intensity of the measured echo will generally plateau, the echo spacing being sufficiently short that the influence of internal gradients upon the signal has become negligible. Finally, we have a CPMG train with

a fixed (short) echo spacing but increasing total time as more RF pulses are added to the train. Hence we have the relaxation dimension, t_3 . The signal attenuation is thus given by

$$S(g_1, t_2, t_3) = \iiint \exp(-\gamma^2 g_1^2 \delta^2 \Delta_r) \exp(-\frac{1}{3} \gamma^2 (Dg^2) t_2^2 \tau) \exp(-t_3 R_2) \\ \times f(D, (Dg^2), R_2) dD d(Dg^2) dR_2 \quad (9.37)$$

where Δ_r is the effective diffusion time.

Notice the importance of the various relevant length scales in our analysis. The dephasing length scale $l_g = (D_0/\gamma g)^{1/3}$ was introduced in Chapter 6. In a porous medium there exists a structural feature length scale, l_s , over which the magnitude of the internal gradient arising from local fields will change. There is also the distance, $l_E = (D_0 \tau_E)^{1/2}$ or $(D_0 t_2)^{1/2}$, diffused over the relevant echo time, τ_E or t_2 . Provided $l_E \ll l_g$, the diffusion-induced echo attenuation between successive pairs of echoes is small, and the cumulative attenuation over many echoes is the result of successively small dephasing. For T_2 encoding through the multi-echo CPMG train, τ_E needs to be sufficiently short that T_2 effects are dominant. And, in order that we might sensibly use a local gradient description such that eqn 9.37 applies, we will require that $l_E \ll l_s$.

As an example of a relaxation local field experiment, Fig. 9.24 shows results obtained for water in a porous rock, where the pulse sequence has two encoding dimensions, inversion recovery for T_1 , and a multi-echo train of variable echo spacing and total fixed time, to encode for Dg^2 . In the interpretation of the data, D is taken to be constant and equal to the molecular self-diffusion coefficient of water. In consequence, a value for g may be derived in the inversion process. The examples shown in Fig. 9.24 feature increasing polarising field B_0 , such that scaling laws for the dependence of T_1 and g on B_0 may be tested.

As B_0 is increased, the effect of susceptibility inhomogeneity is to cause the inhomogeneous local internal fields, $\Delta\chi B_0$, to proportionately increase, along with their local gradients, $\Delta\chi B_0/l_s$. However, there is an upper limit to the effective gradient that can be measured, and this limit is reached when structural features have length scales on the order of l_g . Setting $g_{max} = \Delta\chi B_0/l_s$, where $l_s = l_g$, one finds [41]

$$g_{max} = \left(\frac{\gamma}{D_0} \right)^{1/2} (\Delta\chi B_0)^{3/2} \quad (9.38)$$

with the critical structural length scale being

$$l^* = \left(\frac{D_0}{\gamma \Delta\chi B_0} \right)^{1/2} \quad (9.39)$$

For pores smaller than l^* , the fluctuations in gradient as molecules diffuse mean that the local gradients are averaged over the dephasing length. For larger pores, as l_s begins to approach l^* , the measured effective gradient approaches g_{max} , while for pores larger than l^* , the dephasing of the CPMG signal over the echo time, such that

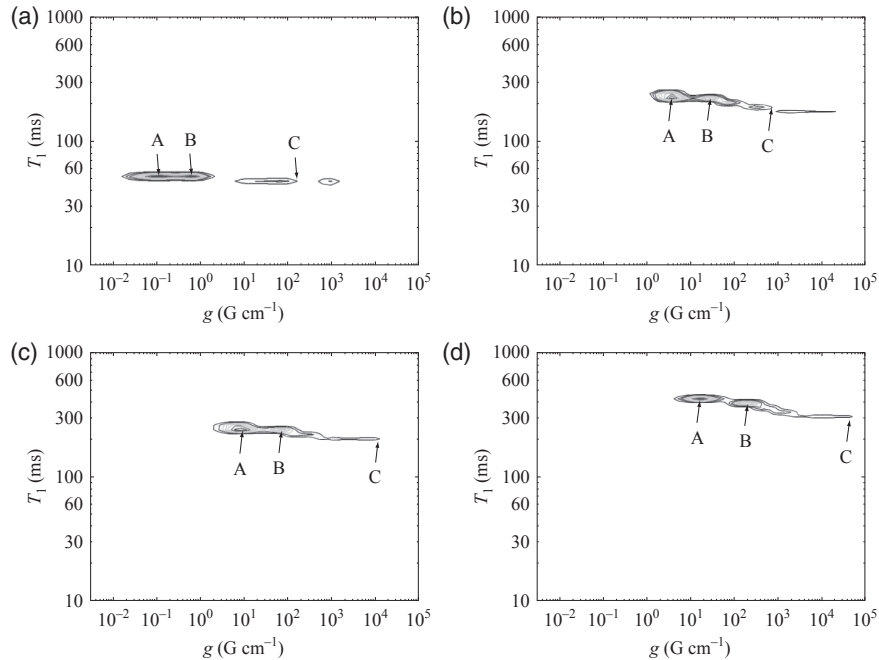


Fig. 9.24 $T_1 - g$ plots for water imbibed in a Mt. Gambier limestone at (a) 12 MHz, (b) 200 MHz, (c) 400 MHz, and (d) 900 MHz proton NMR frequency. A, B, and C arrows indicate the tracked intensity for regions of the 2-D inverse Laplace spectrum corresponding to pores of successively smaller size. Note the increasing local field and lengthening T_1 relaxation time as the Zeeman field applied to the sample is increased. (Reproduced with permission from Washburn *et al.* [38].)

$l_E \ll l_s$, arises from a local gradient that is effectively constant. This is the limit, applicable in eqn 9.37, where the overall echo train attenuation may be calculated by summing the contributions from each part of the distribution of gradients in the ensemble of spins.

9.5.5 DDCOSY

In Chapter 8, Section 8.5.3 introduced the concept of structural domains exhibiting local anisotropy, but where the overall domain distribution exhibits global isotropy. The use of double wavevector encoding as a means of revealing such structural asymmetry was also outlined. In that treatment, the small wavevector limit was presented, under the condition that successive pairs of gradient pulses were applied along common or along different axes. In fact, this type of measurement can be multiplexed, using independent encoding of the gradient pairs to probe orthogonal domains of displacement in a 2-D correlation experiment, a method known as Diffusion–Diffusion COrrelation SpectroscopY or DDCOSY. This technique, where one compares 2-D maps obtained with either collinear or orthogonal gradient pulse pairs, has been applied to the study

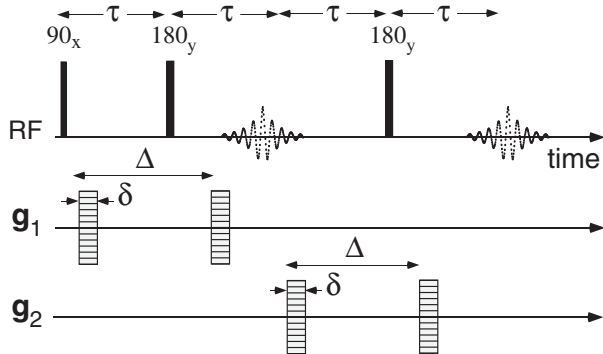


Fig. 9.25 DDCOSY pulsed gradient spin-echo NMR pulse sequence in which two successive pairs of diffusion encoding gradient pulses, with directions either collinear or orthogonal, are stepped independently.

of local diffusional asymmetry in lyotropic liquid crystals. The pulse sequence is given in Fig. 9.25.

In general, we may write the relationship between the signal and the diffusion coefficient distribution as

$$S(g_1, g_2) = \iint \exp(-\gamma^2 g_1^2 \delta^2 D_1 \Delta_r) \exp(-\gamma^2 g_2^2 \delta^2 D_2 \Delta_r) f(D_1, D_2) dD_1 dD_2 \quad (9.40)$$

where, as usual, $\Delta_r = \Delta - \delta/3$. Suppose we take a locally anisotropic diffusion tensor describable by the ellipsoid of revolution of Fig. 8.14. The relevant echo-attenuation expressions for E_{zz} and E_{zx} in the case of the double wavevector encoding, with equal magnitude gradient pulses, are those of eqn 8.45. Here these equations are modified to allow for independent q -vectors \mathbf{q}_1 and \mathbf{q}_2 , such that

$$\begin{aligned} E(q_{1z}, q_{2z}) &= \int_0^1 d \cos \theta \exp(-(q_{1z}^2 + q_{2z}^2) \Delta [D_{\parallel} \cos^2 \theta + D_{\perp} (1 - \cos^2 \theta)]) \\ E(q_{1z}, q_{2x}) &= (2\pi)^{-1} \int_0^1 d \cos \theta \exp(-q_{1z}^2 \Delta [D_{\parallel} \cos^2 \theta + D_{\perp} (1 - \cos^2 \theta)]) \\ &\times \int_0^{2\pi} d\phi \exp(-q_{2x}^2 \Delta [D_{\parallel} (1 - \cos^2 \theta) \cos^2 \phi + D_{\perp} \sin^2 \phi + D_{\perp} \cos^2 \theta \cos^2 \phi]) \end{aligned} \quad (9.41)$$

Equations 9.41 for E_{zz} and E_{zx} provide quite different responses, depending on the successive orientation of the gradient directions. Despite the isotropic distribution of directors, the chance of capturing a fast diffusion direction in either of the two encoding pairs is enhanced when the gradient direction is switched in the second pair. Of course, for a known, axially symmetric, diffusion anisotropy, the diffusion distribution, $f(D_1, D_2)$, can be deduced directly from eqn 9.41. Figure 9.26 shows the result of such a calculation carried out in the case of a prolate local diffusion tensor ($D_{\perp} = 0.1D_{\parallel}$), perhaps describing a ‘random array of pipes’, as well as the oblate

case ($D_{\parallel} = 0.1D_{\perp}$) relevant to a polydomain lamellar phase liquid crystal in which solvent molecules diffuse freely along the lamellae. These ideal distributions become distorted by the pearling process in the inverse Laplace transformation of the echo attenuation data generated using eqn 9.41. Nonetheless, the patterns are reproducible and consistent and, most importantly, highly characteristic of either oblate or prolate symmetry [42].

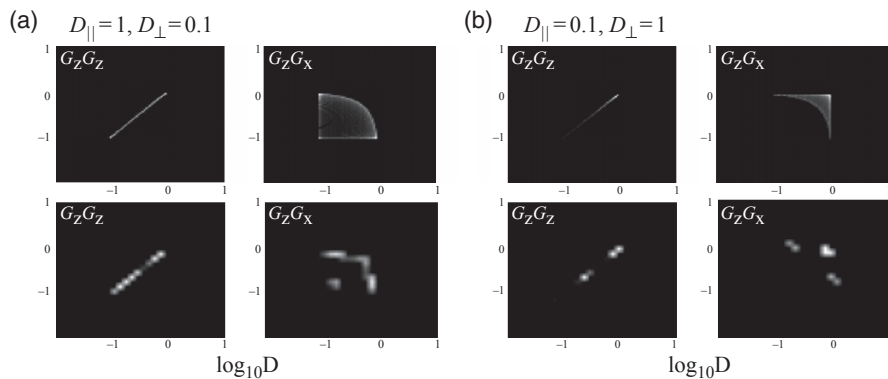


Fig. 9.26 (a) Calculated DDCOSY spectra for isotropic distribution of locally anisotropic diffusion elements in the case $D_{\perp} = 0.1D_{\parallel}$. The upper panels are calculated directly from the analytic distribution of diffusion coefficients apparent in eqn 9.41, while the lower panels are calculated by using eqn 9.41 to generate echo attenuations, which are then subject to 2-D inverse Laplace transformation. Note the distinctive off-diagonal features when the gradient directions are switched. (b) as for (a) but for the case $D_{\parallel} = 0.1D_{\perp}$. (Reproduced with permission from reference [42].)

An experimental demonstration of DDCOSY is shown in Fig. 9.27 in which theory and experiment are compared for water diffusing in a polydomain lamellar phase of the lyotropic liquid crystal, 40 wt % non-ionic surfactant C10E3 ($C_{10}H_{21}O(CH_2CH_2O)_6H$) in H_2O [43]. Strong off-diagonal features are apparent in the case where the successive gradients are applied in orthogonal directions, while a diagonal spectrum is apparent for collinear gradients. The agreement between theory and experiment provides nice confirmation for the existence of a multi-domain lamellar phase. Note that the ‘slow’ and ‘fast’ diffusion limit D_{\parallel} ad D_{\perp} can be read directly from these maps.

Crucially the domain size must be smaller than the diffusive observation time, Δ , if the molecules are to reside in a common domain over the DDCOSY encoding. In the present example $\Delta = 30$ ms corresponding to a water molecule diffusion distance of about $10 \mu\text{m}$. The absence of off-diagonal intensity in the collinear gradient plot provides confirmation that common domain behaviour is observed, and hence the domain size must be larger than this.

The question arises of whether the domain size can be measured by increasing the observation time using the collinear gradient pulse experiment. The answer, of course,

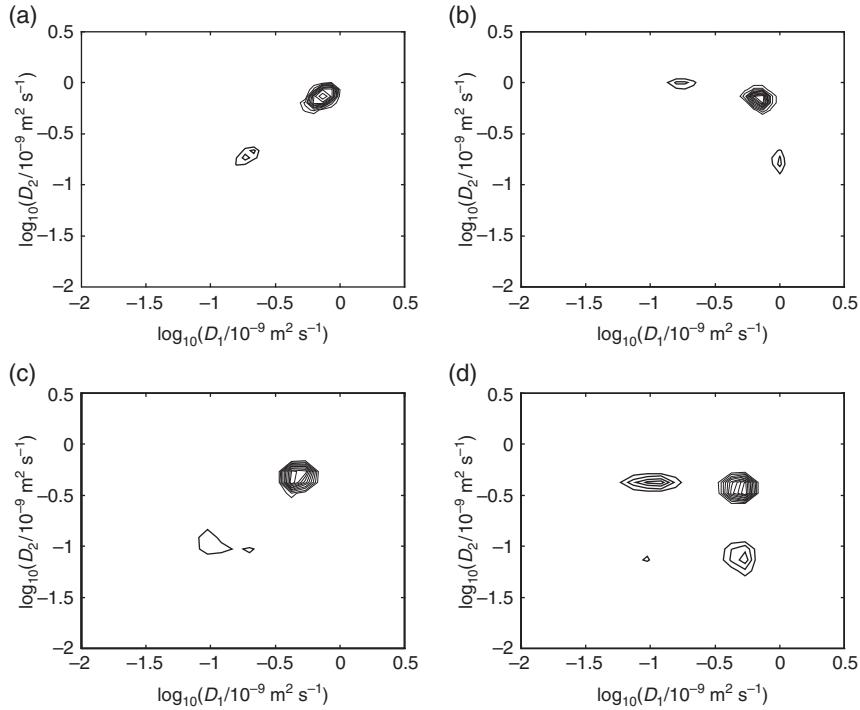


Fig. 9.27 (a) and (b) Calculated DDCOSY spectra for isotropic distribution of locally anisotropic diffusion elements in the case $D_{\parallel} = 0.1D_{\perp}$, with $D_{\perp} = 1 \times 10^{-9} \text{ m}^2 \text{ s}^{-1}$. In (a) the gradient pulse pairs are collinear and in (b) they are orthogonal. The maps are calculated by using eqns 9.41 to generate echo attenuations, which are then subjected to 2-D inverse Laplace transformation. The contours represent a linear intensity scale with ten equal steps. (c) and (d) Equivalent maps but for an actual experiment on water molecules in the polydomain lamellar phase of a 40 wt % C10E3/water sample. (Reproduced with permission from reference [43].)

is ‘yes’, and the ideal way to do this is to maintain Δ short, but to introduce a well-defined mixing time, τ_m , as a delay between the encoding pulse pairs. Thus we move from a correlation experiment to an exchange experiment. Exchange methods are the subject of the next section.

9.6 Multidimensional Laplace–Laplace exchange methods

The measurement of exchange involves encoding for the same property at two different times, in order to ascertain any changes due to system dynamics. Multi-dimensional exchange methods rely on the fact that unchanging parameters will lie along the plot diagonal, while those that change between encodings will move off-diagonal. In order to ensure a common molecular identity for the parameter to be compared, each unique molecular magnetisation participating in the experiment must prevail over the mixing time, τ_m , the time over which the system is allowed to evolve between encodings.

This limits us to mixing times on the order of the slowest relaxation process from which we can protect the spins, typically T_1 , and hence with protection imparted by storing magnetisation along the longitudinal axis. z -storage will be the norm in the experiments to follow.

Measuring the intensity of off-diagonal features as a function of the variable mixing time gives access to the dynamical rate constants. Here, consistent definitions of the region of intensity to be integrated are essential. In multi-dimensional exchange experiments involving the ILT, the effect of pearlring is often to gather intensity into identifiable ‘islands’ in the plot. These can provide just the definition we seek when tracking τ_m -dependence of intensity, but, of course, caution is needed to ensure that sufficient stability is present in the inversion process to justify this type of analysis.

9.6.1 DEXSY

Diffusion Exchange SpectroscopY (DEXSY), compares molecular self-diffusion coefficients after a mixing interval. It is particularly useful for examining systems in which molecules are partitioned according to their diffusive behaviour, but exchange between these partitions over NMR-accessible timescales of milliseconds to seconds. The pulse sequence for DEXSY is essentially the same as that used for the VEXSY experiment and shown in Fig. 9.5. The variant shown here in Fig. 9.28 uses z -storage using the mixing interval, so that the spins experience only the slower T_1 relaxation. For our

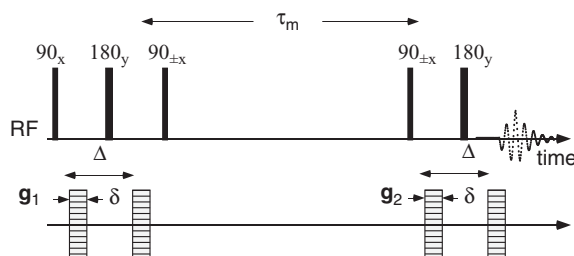


Fig. 9.28 DEXSY PGSE experiment in which two collinear gradient pulses pairs separated by a mixing time τ_m are stepped independently. z -storage of magnetisation is used during the mixing period.

first example of the use of DEXSY, we return to the polydomain lamellar lyotropic 40 wt % C10E3/water phase discussed in the previous section. Water molecules will diffuse over the mixing time and, in doing so, some will reach a new domain, while some will remain at the end of the mixing period in their original domain. For the latter, their signal contribution takes the form of the first of eqns 9.41, which we denote $E(q_{1z}^2, q_{2z}^2)_{orig}$. This signal contributes a completely diagonal DEXSY spectrum when subject to 2-D inverse Laplace transformation. By contrast, molecules that have diffused to a new domain will have a local director completely uncorrelated with their starting director so that their contribution to the echo attenuation is given by

$$\begin{aligned}
E(q_{1z}^2, q_{2z}^2)_{new} = & \int_0^1 d \cos \theta \exp (-q_{1z}^2 \Delta [D_{\parallel} \cos^2 \theta + D_{\perp} (1 - \cos^2 \theta)]) \\
& \times \int_0^1 d \cos \theta \exp (-q_{2z}^2 \Delta [D_{\parallel} \cos^2 \theta + D_{\perp} (1 - \cos^2 \theta)])
\end{aligned} \tag{9.42}$$

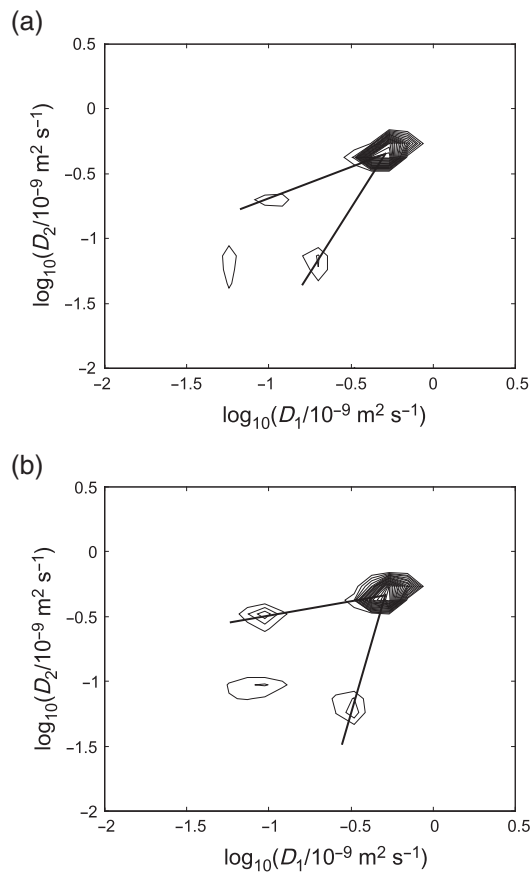


Fig. 9.29 DEXSY (D_1, D_2) exchange maps obtained from water molecules in the polydomain lamellar phase of the 40 wt % C10E3/water sample, using (q_{1z}^2, q_{2z}^2) encoding and in which the total effective mixing time τ'_m is (a) 230 ms and (b) 830 ms (Reproduced with permission from reference [43].)

The relative proportions of each population are determined by diffusion between the lamellar domains. For diffusion coefficient D_{\perp} and given a rms domain size d , the resulting echo-attenuation expression can be written

$$\begin{aligned}
E(q_{1z}^2, q_{2z}^2) = & E(q_{1z}, q_{2z})_{orig} \left(1 - \int_d^\infty 2\pi r dr (\pi D_\perp \tau_m)^{-1} \exp(-r^2/4D_\perp \tau_m) \right) \\
& + E(q_{1z}^2, q_{2z}^2)_{new} \int_d^\infty 2\pi r dr (\pi D_\perp \tau_m)^{-1} \exp(-r^2/4D_\perp \tau_m)
\end{aligned} \tag{9.43}$$

in which r is a 2-D displacement along the lamellae (in the \perp direction). Strictly, τ_m should be replaced with the effective mixing time $\tau'_m = \tau_m + \Delta$. When used to generate 2-D echo-attenuation functions that are subsequently subjected to the ILT, eqn 9.43 yields a map like that shown in Fig. 9.29, on which the off-diagonal peaks subtend an angle that depends on the mixing time [43]. A measurement of that angle enables one to estimate the domain size d . For the data shown in Fig. 9.29, $d \approx 43 \mu\text{m}$.

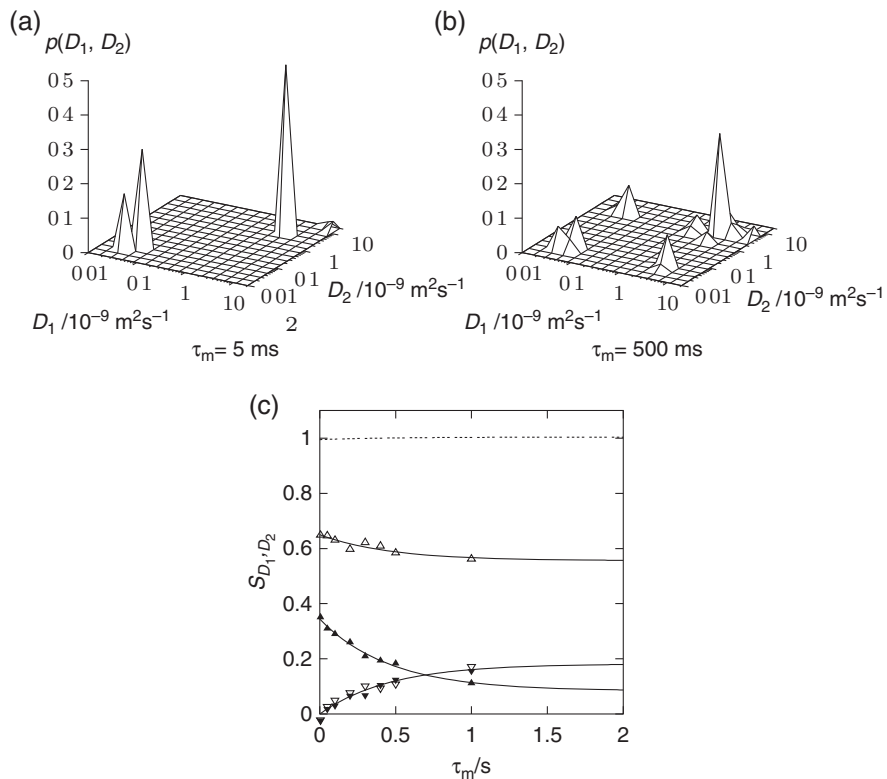


Fig. 9.30 (a) and (b) 2-D inverse Laplace transformed NMR signal maps of DEXSY experiments for pentane in zeolite, at different mixing times τ_m . (c) T_1 and T_2 corrected intensities of both (off-diagonal) exchange peaks (inverted triangles) and the (diagonal) free (open triangles), and adsorbed peaks (filled triangles) acquired by DEXSY, as well as their corresponding fits (—). For the fit of both exchange peaks their mean value was used. The sum of all four fitted intensities is also shown (---). Experimental uncertainties are on the order of the symbol size. (Reproduced with permission from Gratz *et al.* [44].)

The DEXSY method is particularly effective in analysing exchange of diffusing molecules between compartments in a partitioned system. It has been used to study diffusion of dextran with molecular weights 4.4 and 77 kDa through polyelectrolyte multilayer hollow capsules consisting of four bilayers of polystyrene sulfonate/polydiallyl dimethylammonium chloride. Intra-capsule and free dextran diffusion coefficients were identified, with off-diagonal DEXSY peaks arising from dextran migrating between the capsule and solvent spaces, exchange times of around 1 s being found [45].

Another example concerns diffusion of n-pentane between the interior and the exterior of zeolite crystals [44]. These crystals had diameters of around 15 μm , and were loaded with 500 mg g⁻¹ n-pentane (2.5 times the maximum loading) such that there exists both an adsorbed phase (molecules in the zeolite) and a free liquid phase (molecules in the inter-crystalline space). Figure 9.30(a) shows the DEXSY map at short (5 ms) mixing time, where few molecules have time to diffuse between the adsorbed and free liquid phases. Two regions of intensity are seen on the diagonal: one corresponding to free pentane and the other, with much slower diffusion coefficient, to pentane within the zeolite crystals. As the mixing time is increased, as seen in Fig. 9.30(b), off-diagonal peaks arise due to molecules switching phases, and the plot in (c) shows the growth in intensity of these peaks, as well as the corresponding decay of the on-diagonal peaks as the mixing time is increased. Note that the intensities of these peaks has been corrected for both T_1 and T_2 relaxation. Fitting to a simple exponential behaviour yields an exchange time of 460 ± 50 ms, slower than that expected due to diffusion across the known crystal size, and therefore indicative of surface barriers [44].

9.6.2 Relaxation exchange spectroscopy

The very first 2-D ILT experiment carried out by Lee *et al.* [26] concerned T_2 - T_2 exchange. In porous media, spin relaxation rates depend on pore surface-to-volume ratios, and hence can be used to derive pore size distributions [46]. In consequence, the change of spin-relaxation rates as molecules ‘exchange’ from pore to pore provides a window on inter-pore transport. However, the method is equally applicable to other materials, for example in soft matter, with exchange between liquid crystal domains, or in biophysics, where metabolites exchange between the interior and exterior of cells. In each of these it is useful to be able to quantify the details of exchange between specific sub-populations.

As for DEXSY, Relaxation EXchange SpectroscopY (REXSY) correlates molecular properties at two different times—in the pulse sequence shown in Fig. 9.31, their spin–spin (T_2) relaxation rates, preserving the magnetisation of individual molecules over a variable ‘mixing time’, separate the two encoding intervals when relaxation behaviour influences the spin magnetisation. The pulse sequence begins with a 90° RF excitation pulse, followed by the first T_2 encoding, in the form of a CPMG echo train in which the echo time is fixed while the number (n) of refocusing 180° pulses is varied. The use of closely spaced 180° RF pulses avoids any additional dephasing due to diffusion in the local gradients associated with internal diamagnetic susceptibility differences. A second 90° RF stores the magnetisation along the z -axis for the mixing time, τ_m , after which a third 90° RF pulse returns the magnetisation to the transverse plane,

where the second T_2 encoding is efficiently performed in conjunction with multi-echo data acquisition.

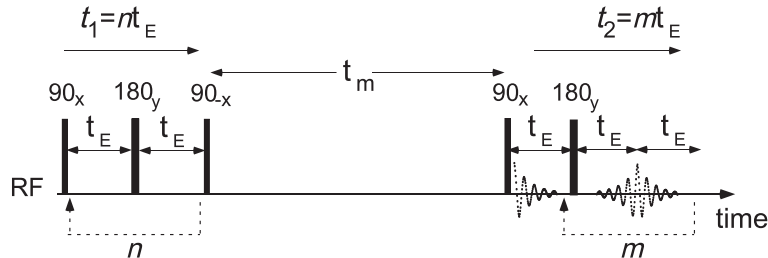


Fig. 9.31 Pulse sequence for the measurement of transverse relaxation exchange. At any fixed time interval τ_E , the numbers (n, m) of 180° RF pulses in the first and second T_2 encoding periods is independently varied. A succession of measurements are then made as a function of the mixing time τ_m .

The first application of the method was by McDonald and Korb [47] and Lee *et al.* [26], who observed T_2 exchange at a fixed time separation. Figure 9.32 shows the results of a variable mixing-time experiment carried out for water imbibed in a Castlegate sandstone [48]. The first T_2 encoding involves 42 logarithmically spaced echo train durations over the range 0.05–51.2 ms, while the second uses single-point acquisition at the top of each of 1024 CPMG echoes, giving a (42×1024) 2-D data set, from which second domain sampling points are chosen to produce a 42×42 matrix for subsequent inverse Laplace transformation. Castlegate sandstone exhibits T_2 relaxation times much shorter than T_1 . However, a T_1 - T_2 correlation experiment was used to assess the T_1 value for each T_2 component so that a correction could be made for longitudinal relaxation during the mixing time z -storage.

Figure 9.32 shows the 2-D T_2 exchange distribution at a mixing time of 160 ms. Along the diagonal, pearlring results in discrete peaks seen at approximately 0.2 ms (labelled A), 1.6 ms (labelled B), 8 ms (labelled C), and 32.6 ms (labelled D). For the 0.2 ms, 1.6 ms, and 8 ms peaks, exchange between T_2 environments can be clearly seen, though no exchange appears between the 32.6 ms peak and those associated with shorter T_2 values. The longest relaxation peak is interpreted as belonging to a ‘bulk’ water phase, from which exchange is very slow.

The data shown in Fig. 9.32 can be analysed to reveal exchange times using the Zimmerman-Brittin method of Section 6.3.1. A somewhat simplistic first-order approach is to overlook the three sites involved and use a binary site model for each exchange peak. For the A–B exchange, the numbers of molecules, $N_{AB}(t)$, starting in A but residing in B after a mixing time t , corresponds to the A–B off-diagonal peak intensity. The rate equation will be $dN_{AB}/dt = N_{AA}/\tau_{AB} - N_{AB}/\tau_{BA}$, where N_{AA} is the number remaining in A after time t , and τ_{AB}^{-1} and τ_{BA}^{-1} are determined by the rates at which molecules in A migrate to B and vice versa. Such rates will be governed by the molecular self diffusion coefficient, the tortuosity of the pore throats, and the inter-pore distance. With initial condition $N_{AB}(0) = 0$, one may write [48]

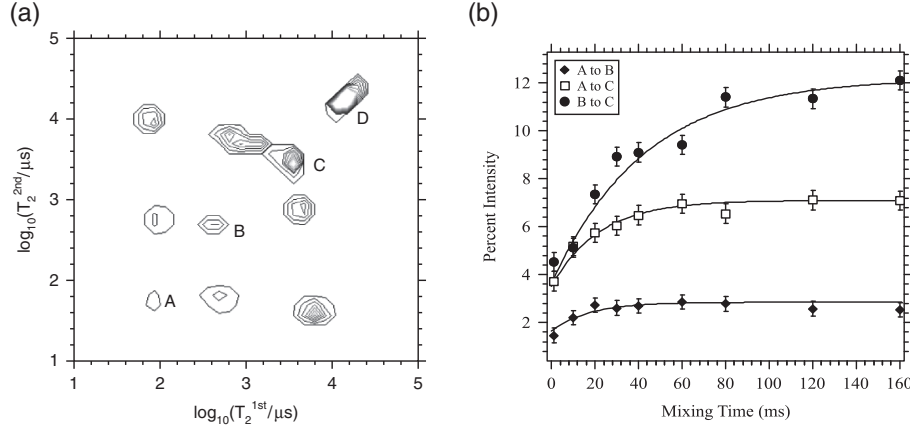


Fig. 9.32 (a) 2-D T_2 exchange distribution for water in Castlegate sandstone at a 160 ms mixing time. (b) Off-diagonal intensities, $N_{\alpha\beta}(t)$, as a function of mixing time.

$$N_{AB}(t) = \frac{N_B \tau_{AB}}{\tau_{AB} + \tau_{BA}} (1 - \exp(-\lambda t)) \quad (9.44)$$

with $\lambda = \tau_{AB}^{-1} + \tau_{BA}^{-1}$ and $\tau_{ex}^{AB} = \lambda^{-1}$. This exponential growth relationship is evident in Fig. 9.32, and using eqn 9.44 the exchange times are found to be $\tau_{ex}^{AB} = 27 \pm 3$ ms, $\tau_{ex}^{AC} = 31 \pm 3$ ms, and $\tau_{ex}^{BC} = 90 \pm 10$ ms. Similar relations can be derived for the exponential decay of the diagonal peaks where a self-consistent set of exchange times are observed.

A nice quantitative validation of REXSY has been carried out by Mitchell *et al.* [49] using a model porous medium comprising mixtures of nonporous borosilicate and soda lime glass spheres (diameter 100 μm) in water, thus providing an approximately constant characteristic pore dimension throughout the structures, but where water in different pore-space regions had significantly different T_2 relaxation rates because of the two glass types. The packed beds were constructed with controlled glass-type domain sizes so as to test a model for region-to-region exchange of water. Using REXSY-determined exchange times along with the known self-diffusion coefficient of water, these authors calculated corresponding length scales that closely corresponded with the known domain dimensions.

9.6.3 Symmetry and peak amplitude sign in exchange and correlation spectroscopy

Single pore multimodes

The multi-eigenmodes of the Brownstein–Tarr relaxation-diffusion problem for a single pore imply the existence of multiple T_1 and T_2 values, except in the fast diffusion limit, $\bar{\rho}a/D \ll 1$, where a is the pore size. Hence, in slow and intermediate diffusion a single pore may return a multi-component $T_2 - T_2$ or $T_1 - T_2$ spectrum. As we have seen in Section 9.5.2, for the $T_1 - T_2$ correlation experiment, where the T_1 and T_2 relaxivities $\bar{\rho}_1$ and $\bar{\rho}_2$ are different, the eigenmodes of the T_1 and T_2 relaxation processes may be non-orthogonal and off-diagonal peaks may occur with negative amplitude [32],

and hence not be amenable to an ILT process based on the non-negative amplitude assumption. Such curious negative peaks correspond to coupling between modes i and j in which $T_2^{(i)} > T_1^{(j)}$, that is, ‘above the diagonal’ of the correlation map if T_2 is the vertical axis. Single-pore $T_2 - T_2$ correlation may also exhibit off-diagonal intensity, provided the pulse sequence includes an intervening T_1 relaxation process between the two T_2 encodings, but for such $T_2 - T_2$ correlation the off-diagonal intensities are always positive and the correlation map symmetric [32].

Diffusion between interconnected pores

For a sample comprising pores of differing sizes, multi-component T_2 or T_1 spectra are found, even for fast exchange in each pore and local single modal relaxation. In this case, the observed relaxation rate provides a pore label based on the local surface-to-volume ratio, as discussed in Section 9.6.2. Here diffusive exchange between interconnected pores results in off-diagonal peaks, but in the case of pure $T_2 - T_2$ exchange, without intervening relaxation, the spectra are necessarily symmetric, and all off-diagonal peaks are positive in amplitude. But if T_1 relaxation occurs during the mixing time, mode admixture can, in principle, lead to negative, albeit weak, off-diagonal peaks [33].

There does exist the possibility of an unusual exchange experiment in which T_1 and T_2 are successively encoded, separated by a mixing time. In the case where diffusion between pores is rapid compared with intrapore diffusion, a common T_1 and T_2 value is found and the $T_1 - T_2$ spectrum exhibits a single peak. Where diffusion between pores is much slower than intrapore diffusion, separate peaks labelling the (T_1, T_2) coordinates of each pore will be found. However, at intermediate exchange rates, cross-peaks will appear. Here again, symmetry is no longer implied for $T_1 - T_2$, and negative off-diagonal peaks are possible [31, 32], but predominantly where $T_2^{(i)} > T_1^{(j)}$ [33]. It is clear that (T_1, T_2) experiments require considerable care in interpretation and that the role of negative amplitude contributions can significantly complicate the use of the standard non-negativity constraint approach to inverse Laplace transformation.

9.7 Diffusion tensor measurement

In Chapter 1, Section 1.3.5, the diffusion tensor was introduced, and its measurement using pulsed magnetic field gradients was discussed briefly in Chapter 5, Section 5.5.5. Acquiring the signals needed to calculate the diffusion tensor involves a multidimensional encoding [50]. Here we expand a little on the discussion in Section 5.5.5 to describe the data processing and methodology in a little more detail.

9.7.1 Frame transformation

Because the random displacements associated with Brownian motion are uncorrelated along orthogonal Cartesian axes, the diffusion tensor, which describes velocity autocorrelation, is intrinsically diagonal. However, in a material medium in which molecules diffuse under conditions of local structural anisotropy, there will exist a principal axis frame associated with that structure, in which the diagonal components of the diffusion tensor are expressed. These numbers D_{11} , D_{22} , and D_{33} give the self-diffusion rates along each of the local structural axes. For example, if our system comprised

water molecules diffusing in a fibrous structure, we might expect that there would be rapid diffusion along the fibre axis, perhaps labelled 1, and slower diffusion transverse to the fibres, along axes 2 and 3. In this case we would have $D_{11} > D_{22} = D_{33}$, the equality representing axial symmetry.

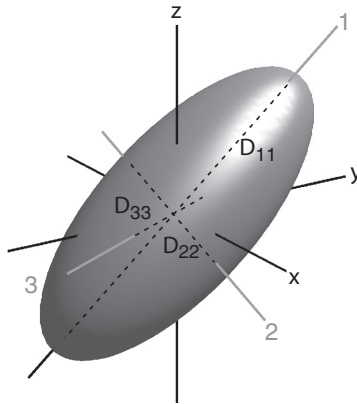


Fig. 9.33 Ellipsoid representation of diffusion tensor showing principal axis frame (1, 2, 3), rotated with respect to the laboratory-frame coordinates (x, y, z). The eigenvalues of the tensor are the diagonal elements, D_{11} , D_{22} , and D_{33} , of $\underline{\underline{D}}_{local}$ in the principal axis frame, and are represented as the semi-axes of the ellipsoid.

In any attempt to measure local diffusion anisotropy using a laboratory-fixed axis frame, in which magnetic field gradients are applied along orthogonal directions within that frame, there is no *a priori* reason why this laboratory frame and the local structural principal axis frame should coincide. Hence the diffusion tensor measured in the lab frame, $\underline{\underline{D}}_{lab}$, will be related to the local diagonal tensor, $\underline{\underline{D}}_{local}$, using the Cartesian rotation matrices, $\underline{\underline{R}}$, by

$$\begin{aligned}\underline{\underline{D}}_{lab} &= \underline{\underline{R}}^T \underline{\underline{D}}_{local} \underline{\underline{R}} \\ &= \underline{\underline{R}}^T \begin{bmatrix} D_{11} & 0 & 0 \\ 0 & D_{22} & 0 \\ 0 & 0 & D_{33} \end{bmatrix} \underline{\underline{R}} \\ &= \begin{bmatrix} D_{xx} & D_{xy} & D_{xz} \\ D_{yx} & D_{yy} & D_{yz} \\ D_{zx} & D_{zy} & D_{zz} \end{bmatrix} \quad (9.45)\end{aligned}$$

where $\underline{\underline{R}}$ transforms a vector in the laboratory frame to the local frame. Given eqn 9.45, it is obvious that $\underline{\underline{D}}_{lab}^T = \underline{\underline{D}}_{lab}$ or, in other words, $D_{\alpha\beta} = D_{\beta\alpha}$. Clearly only six elements of $\underline{\underline{D}}_{lab}$ are independent, but that represents a considerable increase over the three diffusion coefficients of the local frame, a consequence of not knowing the orientation of the principal axis frame in advance. The extra information we acquire in measuring these extra elements allows us to determine the local frame orientation.

Hence the process for finding D_{11} , D_{22} , and D_{33} involves the following steps. First, PGSE NMR experiments are performed using six linearly independent gradient directions in the (x, y, z) frame. By analysing those experiments, the independent coefficients D_{xx} , D_{xy} , D_{xz} , D_{yy} , D_{yz} , and D_{zz} are obtained, and $\underline{\underline{D}}_{lab}$ constructed. This laboratory-frame matrix is then diagonalised by solving the eigenvalue problem, the eigenvalues being D_{11} , D_{22} , and D_{33} , and the eigenvector transformations being given by the rotation \underline{R} . At this point, the local diffusion anisotropy is known, along with the laboratory-frame directions of the local principal axes.

9.7.2 Echo experiment for diffusion tensor

Following eqns 5.73 and 5.74, allowing that for echo formation at time t the effective gradient $\mathbf{g}^*(t')$ obeys $\int_0^t \mathbf{g}^*(t')dt' = 0$, and neglecting flow, we have for the transverse magnetisation at the echo maximum,

$$M_+(t) = M_+(0) \exp(-\gamma^2 \int_0^t \left[\int_0^{t'} \mathbf{g}^*(t'') dt'' \right]^T \underline{\underline{D}} \left[\int_0^{t'} \mathbf{g}^*(t'') dt'' \right] dt') \exp(-t/T_2) \quad (9.46)$$

where the effective gradient vector is $\mathbf{g}^*(t) = (g_x^*(t), g_y^*(t), g_z^*(t))^T$.

The standard approach to measuring $\underline{\underline{D}}$ is to employ a Stejskal–Tanner PGSE sequence where the effective gradient consists of two identical pulses of opposite sign. Suppose we consider PGSE gradient pulses of duration δ , separation Δ , and amplitude $\mathbf{g} = g\hat{\mathbf{g}}$, the latter represented by a magnitude g and with a direction determined by unit vector $\hat{\mathbf{g}}$. Following a convention used in diffusion measurement, we may write $b = \gamma^2 \delta^2 g^2 (\Delta - \delta/3)$, and so the normalised (to $g = 0$) echo amplitude may be written

$$\begin{aligned} E(\mathbf{g}) &= \exp(-b\hat{\mathbf{g}}^T \underline{\underline{D}} \hat{\mathbf{g}}) \\ &= \exp(-b [\hat{g}_x^2 D_{xx} + \hat{g}_y^2 D_{yy} + \hat{g}_z^2 D_{zz} + 2\hat{g}_x \hat{g}_y D_{xy} + 2\hat{g}_x \hat{g}_z D_{xz} + 2\hat{g}_y \hat{g}_z D_{yz}]) \end{aligned} \quad (9.47)$$

where we have taken advantage of the symmetry of the diffusion tensor, $D_{\alpha\beta} = D_{\beta\alpha}$.

Alternatively we may define a ‘ b -matrix’, given by

$$\begin{aligned} \underline{\underline{b}} &= b \begin{pmatrix} \hat{g}_x \\ \hat{g}_y \\ \hat{g}_z \end{pmatrix} \begin{pmatrix} \hat{g}_x & \hat{g}_y & \hat{g}_z \end{pmatrix} \\ &= b \begin{pmatrix} \hat{g}_x^2 & \hat{g}_x \hat{g}_y & \hat{g}_x \hat{g}_z \\ \hat{g}_y \hat{g}_x & \hat{g}_y^2 & \hat{g}_y \hat{g}_z \\ \hat{g}_z \hat{g}_x & \hat{g}_z \hat{g}_y & \hat{g}_z^2 \end{pmatrix} \end{aligned} \quad (9.48)$$

with

$$E(\underline{\underline{b}}) = \exp(-\underline{\underline{b}} : \underline{\underline{D}}) \quad (9.49)$$

and, taking advantage of the symmetry of the b -matrix elements,⁶

$$\underline{\underline{b}} : \underline{\underline{D}} = b_{xx} D_{xx} + b_{yy} D_{yy} + b_{zz} D_{zz} + 2b_{xy} D_{xy} + 2b_{xz} D_{xz} + 2b_{yz} D_{yz} \quad (9.50)$$

⁶ $b_{\alpha\beta} = b\hat{g}_\alpha \hat{g}_\beta$.

9.7.3 Choice of diffusion gradient directions

A least six different gradient directions $\hat{\mathbf{g}}_i = (\hat{g}_{ix}, \hat{g}_{iy}, \hat{g}_{iz})$ will be needed to find the six independent elements of $\underline{\underline{D}}$. For any given direction, b may be varied, and the local image element signal analysed, in the standard manner of the Stejskal–Tanner experiment, through least squares fitting of $\ln(E)$ vs b , to find the effective diffusion coefficient D_i , where

$$D_i = \hat{g}_{ix}^2 D_{xx} + \hat{g}_{iy}^2 D_{yy} + \hat{g}_{iz}^2 D_{zz} + 2\hat{g}_{ix}\hat{g}_{iy}D_{xy} + 2\hat{g}_{ix}\hat{g}_{iz}D_{xz} + 2\hat{g}_{iy}\hat{g}_{iz}D_{yz} \quad (9.51)$$

From the $i = 1\dots6$ set of simultaneous linear equations for each of the six directions $\hat{\mathbf{g}}_i$, the six independent tensor elements, $D_{\alpha\beta}$, may be simply found. In a series of nice review papers on diffusion tensor imaging, Kingsley [51–53] has provided some direct matrix inversion routes to least squares and weighted least squares calculations of $D_{\alpha\beta}$, in the case where six or more directions are chosen for $\hat{\mathbf{g}}_i$.

The choice of diffusion gradient vectors will be determined by the need for linear independence of the vectors and, where slow diffusion is to be observed, a desire to optimise gradient strength, combinations of x , y , and z gradients providing a larger available gradient magnitude than can be obtained from any single direction. A detailed discussion of the various possible choices, and their respective advantages, is given in reference [52]. One commonly used choice is the set shown in Table 9.1, along with the corresponding matrix elements for b .

$u = 0$ cannot work, as it provides only three different gradient directions. $u = 1$ provides an efficient scheme, corresponding to six pairs of equal-magnitude gradients. $u = \frac{1}{2}(\sqrt{5}+1)$ or $u = \frac{1}{2}(\sqrt{5}-1)$ produces gradients pointing to the vertices of a regular icosahedron [54]. A nice feature of the set shown in Table 9.1 is that, having found the

Table 9.1 Calculation of the b -matrix for a common six-direction diffusion tensor gradient-encoding scheme, showing gradient unit vectors and associated b -matrix elements.

Direction index	\hat{g}_x	\hat{g}_y	\hat{g}_z	b_{xx}	b_{yy}	b_{zz}	b_{xy}	b_{xz}	b_{yz}
1	$\frac{1}{\sqrt{1+u^2}}$	$\frac{u}{\sqrt{1+u^2}}$	0	$\frac{b}{1+u^2}$	$\frac{bu^2}{1+u^2}$	0	$\frac{bu}{1+u^2}$	0	0
2	$\frac{1}{\sqrt{1+u^2}}$	$\frac{-u}{\sqrt{1+u^2}}$	0	$\frac{b}{1+u^2}$	$\frac{bu^2}{1+u^2}$	0	$\frac{-bu}{1+u^2}$	0	0
3	0	$\frac{1}{\sqrt{1+u^2}}$	$\frac{u}{\sqrt{1+u^2}}$	0	$\frac{b}{1+u^2}$	$\frac{bu^2}{1+u^2}$	0	0	$\frac{bu}{1+u^2}$
4	0	$\frac{1}{\sqrt{1+u^2}}$	$\frac{-u}{\sqrt{1+u^2}}$	0	$\frac{b}{1+u^2}$	$\frac{bu^2}{1+u^2}$	0	0	$\frac{-bu}{1+u^2}$
5	$\frac{u}{\sqrt{1+u^2}}$	0	$\frac{1}{\sqrt{1+u^2}}$	$\frac{bu^2}{1+u^2}$	0	$\frac{b}{1+u^2}$	0	$\frac{bu}{1+u^2}$	0
6	$\frac{-u}{\sqrt{1+u^2}}$	0	$\frac{1}{\sqrt{1+u^2}}$	$\frac{bu^2}{1+u^2}$	0	$\frac{b}{1+u^2}$	0	$\frac{-bu}{1+u^2}$	0

effective diffusion coefficients, D_i , corresponding to each of the $i = 1\dots6$ experiments, one may write down the diffusion matrix directly as [53].

$$\begin{aligned} D_{xx} &= h [D_1 + D_2 - u^2(D_3 + D_4) + u^4(D_5 + D_6)] \\ D_{yy} &= h [D_3 + D_4 - u^2(D_5 + D_6) + u^4(D_1 + D_2)] \\ D_{zz} &= h [D_5 + D_6 - u^2(D_1 + D_2) + u^4(D_3 + D_4)] \\ D_{xy} &= (D_1 - D_2)(1 + u^2)/4u \\ D_{xz} &= (D_3 - D_4)(1 + u^2)/4u \\ D_{yz} &= (D_5 - D_6)(1 + u^2)/4u \end{aligned} \quad (9.52)$$

where $h = (1 + u^2)/[2(1 + u^6)]$.

9.7.4 Diagonalisation and diffusion matrix parameters

The diffusion tensor is diagonalised by solving for the eigenvalues, D_{ii} , thus yielding the diagonal diffusion matrix, $\underline{\underline{D}}_{local}$ in its natural principal axis frame. The transformation from the laboratory frame to the principal axis frame is via a rotation matrix $\underline{\underline{R}}$, as shown in eqn 9.45. A suitable $\underline{\underline{R}}$ corresponds to an Euler rotation of coordinates footnoteFollowing convention, as successively rotated axes. successively α about z , β about y , and ζ about z so that

$$\underline{\underline{R}} = \begin{pmatrix} \cos \gamma & \sin \gamma & 0 \\ -\sin \gamma & \cos \gamma & 0 \\ 0 & 0 & 1 \end{pmatrix} \begin{pmatrix} \cos \beta & 0 & -\sin \beta \\ 0 & 1 & 0 \\ \sin \beta & 0 & \cos \beta \end{pmatrix} \begin{pmatrix} \cos \alpha & \sin \alpha & 0 \\ -\sin \alpha & \cos \alpha & 0 \\ 0 & 0 & 1 \end{pmatrix} \quad (9.53)$$

Defining $D_{ave} = \frac{1}{3}[D_{11} + D_{22} + D_{33}]$, the fractional diffusion anisotropy (FA) is

$$\begin{aligned} FA &= \sqrt{\frac{3[(D_{11} - D_{ave})^2 + (D_{22} - D_{ave})^2 + (D_{33} - D_{ave})^2]}{2[D_{11}^2 + D_{22}^2 + D_{33}^2]}} \\ &= \sqrt{\frac{3[(D_{xx} - D_{ave})^2 + (D_{yy} - D_{ave})^2 + (D_{zz} - D_{ave})^2 + 2(D_{xy}^2 + D_{xz}^2 + D_{yz}^2)]}{2[D_{xx}^2 + D_{yy}^2 + D_{zz}^2 + 2(D_{xy}^2 + D_{xz}^2 + D_{yz}^2)]}} \end{aligned} \quad (9.54)$$

Because of the invariance of the trace under a similarity transformation, $D_{ave} = \frac{1}{3}[D_{xx} + D_{yy} + D_{zz}]$. Conveniently, for the gradient directions chosen in Table 9.1, the average diffusion coefficient is given by

$$\begin{aligned} D_{ave} &= \frac{1}{3}[D_{xx} + D_{yy} + D_{zz}] \\ &= \frac{1}{6}[D_1 + D_2 + D_3 + D_4 + D_5 + D_6] \end{aligned} \quad (9.55)$$

Note that FA ranges from 0 for isotropic diffusion ($D_{11} = D_{22} = D_{33}$) to 1 for completely anisotropic diffusion ($D_{11} \neq 0, D_{22} = D_{33} = 0$).

Many more physical properties can be extracted from the diffusion matrix [53]. However, in addition to the average diffusion coefficient, the most important of these is undoubtedly the FA, which informs on the ‘directedness’ of the diffusion process, and, through a knowledge of \underline{R} , the orientation of the principal axis system and hence the local structural orientation of the material with respect to the laboratory frame.

9.7.5 Diffusion tensor imaging

Because diffusional anisotropy provides such a powerful insight regarding local structure in materials or biological tissue, measurement of the diffusion tensor is almost invariably combined with MRI, and commonly known as diffusion tensor imaging (DTI). In medical applications, DTI can be used to follow the pathways of nerve fibres [55] to ascertain muscle orientation, and to determine the structural integrity of brain matter or indicate brain disease [56]. An example of a simple pulse sequence used in DTI is shown in Fig. 9.34, where the pulsed gradients used for diffusion encoding are labelled g_x , g_y , and g_z .

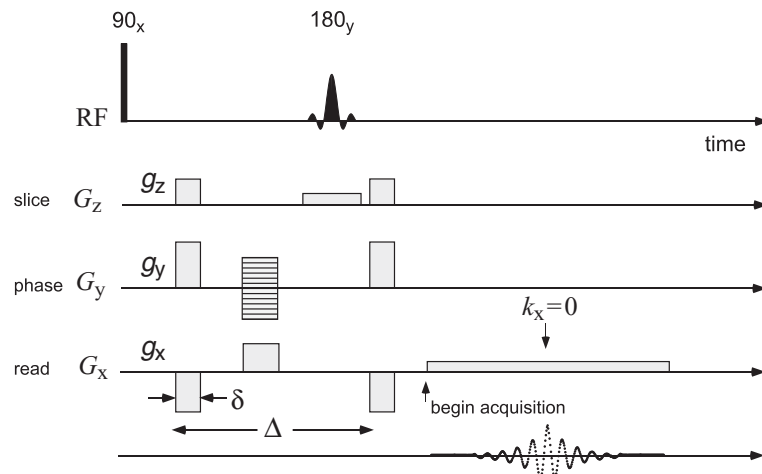


Fig. 9.34 DTI pulse sequence, based on spin warp with a soft 180° RF pulse for slice selection, in which the imaging gradients G_x , G_y , and G_z are supplemented by pulsed gradients g_x , g_y , and g_z , which are stepped from zero to provide the attenuation response arising from diffusion over time Δ . The direction of these diffusion gradients is determined by the vector $(g_x, g_y, g_z)^T$

The echo signal is, of course, encoded in both k - and q -space. The idealised Stejskal–Tanner DTI pulse sequence of Fig. 9.34 yields a multidimensional signal dependent on \mathbf{k} and \mathbf{g} . Using the spin density function $\rho(\mathbf{r})$ to represent local transverse magnetisation $M_+(\mathbf{r})$ in the absence of the PGSE gradients,

$$S(\mathbf{k}, \mathbf{g}) = \int \rho(\mathbf{r}) \exp(i\mathbf{k} \cdot \mathbf{r}) \exp(-b\hat{\mathbf{g}}^T \underline{\underline{D}}(\mathbf{r}) \hat{\mathbf{g}}) d\mathbf{r}, \quad (9.56)$$

$\underline{D}(\mathbf{r})$ being a spatially varying diffusion tensor, which may be used to report on local structural properties. Note that $\rho(\mathbf{r})$ will be influenced by T_2 relaxation over the spin warp sequence, as well as diffusive effects due to the imaging gradient $\mathbf{G}(t)$. These effects are discussed further in Section 9.7.6.

Subsequent to the image reconstruction (Fourier transformation with respect to \mathbf{k}) the local image element signals, $S(\mathbf{r}, \mathbf{g})$, for $b \neq 0$ and $S(\mathbf{r}, 0)$ when $b = 0$, are related by

$$S(\mathbf{r}, \mathbf{g}) = S(\mathbf{r}, 0) \exp(-b\hat{\mathbf{g}}^T \underline{D}\hat{\mathbf{g}}) \quad (9.57)$$

where \underline{D} is implicitly $\underline{D}(\mathbf{r})$, the local diffusion tensor at \mathbf{r} .

9.7.6 Cancelling the effect of imaging gradients

If we analyse the response of the image to the stepping of the PGSE gradients \mathbf{g} , the relaxation attenuation and diffusive attenuation effects quadratic in \mathbf{G} but independent of \mathbf{g} will have no influence. They can, in effect, be normalised out by taking the ratio of the image with that obtained when $\mathbf{g} = 0$. However, the interaction of the imaging and PGSE gradients does involve sensitivity to diffusion due to bilinear terms, $g_\alpha G_\beta$. Clearly then, such artifacts in $E(\mathbf{k}, \mathbf{g})$ will depend (in the exponent) on the sign of \mathbf{g} , while the desired diffusion effect will depend only on \mathbf{g}^2 . One simple means of removing these artifacts [58] is to carry out encodings with both positive and negative PGSE gradients, taking the corrected echo signal as

$$E_{corr}(\mathbf{k}, \mathbf{g}) = (E(\mathbf{k}, \mathbf{g})E(\mathbf{k}, -\mathbf{g}))^{1/2} \quad (9.58)$$

In DTI applications it is customary to apply such a correction.

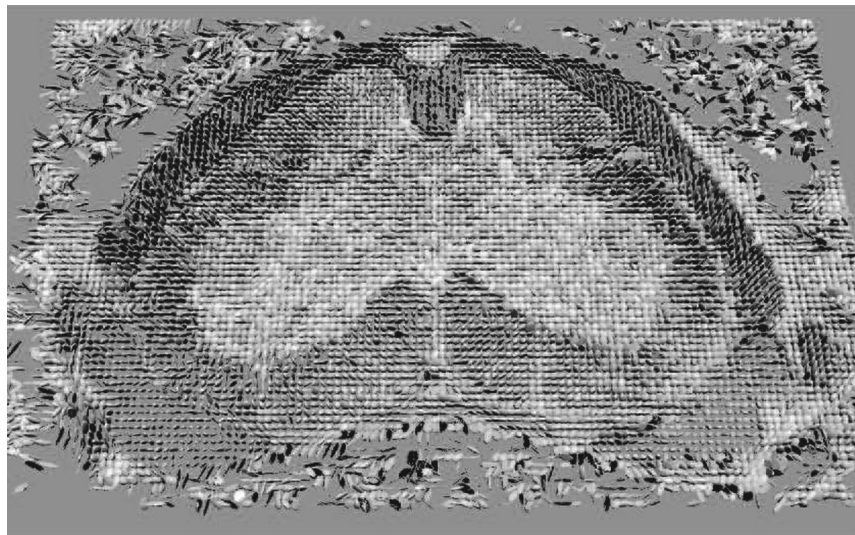


Fig. 9.35 Ellipsoid representation of mouse spinal cord. Note that right–left asymmetries in this image are due to disease. Significant changes are particularly noticeable in the ellipsoid shapes in the myelinated regions in the lower right quadrant of the image. (Reproduced by permission from Laidlaw *et al.* [57].)

9.7.7 Extracting and displaying the information content

One of the biggest difficulties in DTI concerns how to display the spatially resolved tensor quantities. Pierpaoli and Basser [59] have proposed the use of ellipsoids, the semi-axes of which are proportional to the three diffusion eigenvalues, and which have an orientation set to the local principal axis frame. While these are quite informative individually, in a 3-D image the method does present problems. When visualising each voxel in the image dataset, only the outermost layer can be displayed on the screen, with internal data points being hidden. Second, ellipsoids will vary in size, according to D_{ave} , and so may overlap between voxels, making it hard to identify the continuity inherent in biological tissues [60]. One approach is to use normalised ellipsoids, where the largest dimensions are identical, irrespective of D_{ave} , so that they may be scaled to just fill each voxel without overlapping. An example is shown in the mouse spinal cord DTI image shown in Fig. 9.35.

References

- [1] B. J. Davies. *Integral transforms and their Applications*. Springer-Verlag, Berlin, New York, 2002.
- [2] E. I. Fredholm. Sur une classe d'équations fonctionnelles. *Acta Mathematica*, 27:365, 1903.
- [3] I. S. Gradshteyn and I. M. Ryzhik. *Tables of Integrals, Series, and Products*. Academic Press, San Diego, 2000.
- [4] S. J. Provencher. A constrained regularization method for inverting data represented by linear algebraic or integral equations. *Computer Physics Communications*, 27:213, 1982.
- [5] A. N. Tychonoff and V. Y. Arsenin. *Solution of Ill-posed Problems*. Winston and Sons, Washington, 1977.
- [6] S. W. Provencher. CONTIN: A general purpose constrained regularization program for inverting noisy linear algebraic and integral equations. *Comput. Phys. Commun.*, 7:229, 1982.
- [7] K. P. Whittall and A. L. MacKay. Quantitative interpretation of NMR relaxation data. *J. Magn. Reson.*, 84:134, 1989.
- [8] M. Prange and Y-Q. Song. Quantifying uncertainty in NMR T2 spectra using Monte Carlo inversion. *J. Magn. Reson.*, 196:54, 2009.
- [9] L. Venkataramanan, Y-Q. Song, and M. D. Hüerlimann. Solving Fredholm integrals of the first kind with tensor product structure in 2 and 2.5 dimensions. *IEEE Transactions in Signal Processing*, 50:1017, 2002.
- [10] P. T. Callaghan and B. Manz. Velocity exchange spectroscopy. *J. Magn. Reson. A*, 106:260, 1993.
- [11] A. A. Khripitchev, S. Staph, and P. T. Callaghan. NMR visualization of displacement correlations for flow in porous media. *Phys. Rev. E*, 66:051203, 2002.
- [12] S. Staph, R. A. Damion, and K. J. Packer. Time correlations in fluid transport obtained by sequential rephasing gradient pulses. *J. Magn. Reson.*, 137:316, 1999.
- [13] B. Bluemich, P. T. Callaghan, R. A. Damion, S. Han, A. A. Khripitchev, K. J. Packer, and S. Staph. Two-dimensional NMR of velocity exchange: VEXSY and SERPENT. *J. Magn. Reson.*, 152:162, 2001.

- [14] S-I. Han, S. Stapf, and B. Bluemich. Two-dimensional PFG NMR for encoding correlations of position, velocity, and acceleration in fluid transport. *J. Magn. Reson.*, 146:169, 2000.
- [15] S. Stapf, K. J. Packer, R. G. Graham, J-F. Thovert, and P. M. Adler. Spatial correlations and dispersion for fluid transport through packed glass beads studied by pulsed field-gradient NMR. *Phys. Rev. E*, 58:6206, 1998.
- [16] G. P. Wadsworth and J. G. Bryan. *Introduction to Probability and Random Variables*. McGraw-Hill, New York, 1960.
- [17] L. M. Burcaw and P. T. Callaghan. Observation of molecular migration in porous media using 2D exchange spectroscopy in the inhomogeneous magnetic field. *J. Magn. Reson.*, 198:167, 2009.
- [18] L. M. Burcaw and P. T. Callaghan. Propagator resolved 2D exchange in porous media in the inhomogeneous magnetic field. *J. Magn. Reson.*, 205:209–215, 2010.
- [19] J. Jeener, B. H. Meier, P. Bachmann, and R. R. Ernst. Investigation of exchange processes by two-dimensional NMR spectroscopy. *J. Chem. Phys.*, 71:4546, 1979.
- [20] P. Stilbs. Molecular self-diffusion coefficients in Fourier transform nuclear magnetic resonance spectrometric analysis of complex mixtures. *Anal. Chem.*, 53:2135, 1981.
- [21] K. F. Morris and C. S. Johnson. Resolution of discrete and continuous molecular size distributions by means of diffusion-ordered 2D NMR spectroscopy. *J. Am. Chem. Soc.*, 115:4291, 1993.
- [22] P. Stilbs, K. Paulsen, and P. C. Griffiths. Global least-squares analysis of large, correlated spectral data sets: Application to component-resolved FT-PGSE NMR spectroscopy. *J. Phys. Chem.*, 100:8180, 1996.
- [23] S. J. Gibbs and C. S. Johnson. A PFG NMR experiment for accurate diffusion and flow studies in the presence of eddy currents. *J. Magn. Reson.*, 93:395, 1991.
- [24] M. M. Britton, R. G. Graham, and K. J. Packer. NMR relaxation and pulsed field gradient study of alginate bead porous media. *J. Magn. Reson.*, 169:203, 2004.
- [25] A. D. Booth and K. J. Packer. Magnetic spin lattice relaxation in the presence of spin-diffusion. the one-dimensional, two-region system. *J. Magn. Reson.*, 62:811, 1987.
- [26] J-H. Lee, C. Labadie, C. S. Springer, and G. S. Harbison. Two-dimensional inverse Laplace transform NMR: Altered relaxation times allow detection of exchange correlation. *J. Am. Chem. Soc.*, 115:7761, 1993.
- [27] Y-Q. Song, L. Venkataraman, M. D. Hürlimann, M. Flaum, P. Frulla, and C. Straley. T1 T2 correlation spectra obtained using a fast two-dimensional Laplace inversion. *J. Magn. Reson.*, 154:261, 2002.
- [28] M. D. Hürlimann, L. Venkataraman, and C. Flaum. The diffusion-spin relaxation time distribution function as an experimental probe to characterize fluid mixtures in porous media. *J. Chem. Phys.*, 117:10223, 2002.
- [29] M. D. Hürlimann and L. Venkataraman. Quantitative measurement of two-dimensional distribution functions of diffusion and relaxation in grossly inhomogeneous fields. *J. Magn. Reson.*, 157:31, 2002.
- [30] P. T. Callaghan and I. Furó. Diffusion-diffusion correlation and exchange as a signature for local order and dynamics. *J. Chem. Phys.*, 120:4032, 2004.

- [31] L. Monteilhet, J-P. Korb, J. Mitchell, and P. J. McDonald. Observation of exchange of micropore water in cement pastes by two-dimensional T₂-T₂ nuclear magnetic resonance relaxometry. *Phys. Rev. E*, 74:061404, 2006.
- [32] Y-Q. Song, L. Zielinski, and S. Ryu. Two-dimensional NMR of diffusion systems. *Phys. Rev. Lett.*, 100:248002, 2008.
- [33] S. Rodts and D. Bytchenkoff. Structural properties of 2d NMR relaxation spectra of diffusive systems. *J. Magn. Reson.*, 205:315, 2010.
- [34] M. D. Hürlimann, M. Flaum, L. Venkataraman, C. Flaum, R. Freedman, and G. J. Hirasaki. Diffusion-relaxation distribution functions of sedimentary rocks in different saturation states. *Magn. Reson. Imaging.*, 21:305, 2003.
- [35] S-W. Lo, G. J. Hirasaki, W. V. House, and R. Kobayashi. Mixing rules and correlations of NMR relaxation time with viscosity, diffusivity, and gas/oil ratio of methane/hydrocarbon mixtures. *Soc. Petroleum Eng. J.*, 7:24, 2002.
- [36] P. T. Callaghan, S. Godefroy, and B. N. Ryland. Diffusion-relaxation correlation in simple pore structures. *J. Magn. Reson.*, 162:320, 2003.
- [37] B. Sun and K.-J. Dunn. Probing the internal field gradients of porous media. *Phys. Rev. E*, 65:051309, 2004.
- [38] K. E. Washburn, C. D. Eccles, and P. T. Callaghan. The dependence on magnetic field strength of correlated internal gradient-relaxation time distributions in heterogeneous materials. *J. Magn. Reson.*, 194:33, 2008.
- [39] J. G. Seland, K. E. Washburn, H. W. Anthonsen, and J. Krane. Correlations between diffusion, internal magnetic field gradients, and transverse relaxation in porous systems containing oil and water. *Phys. Rev. E*, 70:051305, 2004.
- [40] C. H. Arns, K. E. Washburn, and P. T. Callaghan. Multidimensional NMR inverse Laplace spectroscopy in petrophysics. *Petrophysics*, 48:380, 2007.
- [41] M. D. Hürlimann. Effective gradients in porous media due to susceptibility differences. *J. Magn. Reson.*, 131:232, 1998.
- [42] P. T. Callaghan, S. Godefroy, and B. N. Ryland. Use of the second dimension in PGSE NMR studies of porous media. *Magn. Reson. Imaging*, 21:243, 2003.
- [43] P. T. Callaghan and I. Furó. Diffusion-diffusion correlation and exchange as a signature for local order and dynamics. *J. Chem. Phys.*, 120:4032, 2004.
- [44] M. Gratz, M. Wehring, P. Galvosas, and F. Stallmach. Multidimensional NMR diffusion studies in microporous materials. *Microporous and Mesoporous Materials*, 125:30, 2009.
- [45] Y. Qiao, P. Galvosas, T. Adalsteinsson, M. Schoenhoff, and P. T. Callaghan. Multidimensional NMR diffusion studies in microporous materials. *J. Chem. Phys.*, 122:214912, 2005.
- [46] R. L. Kleinberg and M. A. Horsfield. Transverse relaxation processes in porous sedimentary rock. *J. Magn. Reson.*, 88:9, 1990.
- [47] P. J. McDonald, J-P. Korb, and L. Monteilhet. Surface relaxation and chemical exchange in hydrating cement pastes: A two-dimensional NMR relaxation study. *Phys. Rev. E*, 72:011409, 2005.
- [48] K. E. Washburn and P. T. Callaghan. Tracking pore to pore exchange using relaxation exchange spectroscopy. *Phys. Rev. Lett.*, 97:175502, 2006.

450 Multidimensional PGSE NMR

- [49] J. Mitchell, J. D. Griffith, J. H. P. Collins, A. J. Sederman, L. F. Gladden, and M. L. Johns. Validation of NMR relaxation exchange time measurements in porous media. *J. Chem. Phys.*, 127:234701, 2007.
- [50] P. J. Basser, J. Mattiello, and D. LeBihan. MR diffusion tensor spectroscopy and imaging. *Biophysical Journal*, 66:259, 1994.
- [51] P. B. Kingsley. Introduction to diffusion tensor imaging mathematics: Part I. Tensors, rotations, and eigenvectors. *Concepts Magn. Reson.*, 28A:101, 2005.
- [52] P. B. Kingsley. Introduction to diffusion tensor imaging mathematics: Part II. Anisotropy, diffusion-weighting factors, and gradient encoding schemes. *Concepts Magn. Reson.*, 28A:123, 2005.
- [53] P. B. Kingsley. Introduction to diffusion tensor imaging mathematics: Part III. Tensor calculation, noise, simulations, and optimization. *Concepts Magn. Reson.*, 28A:155, 2005.
- [54] K. M. Hasab, D. L. Parker, and A. L. Alexander. Comparison of gradient encoding schemes for diffusion-tensor MRI. *J. Magn. Reson. Imaging*, 13:769, 2001.
- [55] P. J. Basser. *Magnetic resonance imaging of the brain and spine*, chapter Diffusion and diffusion tensor MR imaging. J.J. Attard ed., Lippincott, Williams and Wilkin, Philadelphia, 2002.
- [56] M. Moseley. Diffusion tensor imaging and aging—A review. *NMR Biomed.*, 15:553, 2002.
- [57] D. H. Laidlaw, E. T. Ahrens, D. Kremers, M. J. Avalos, R. E. Jacobs, and C. Readhead. Visualizing diffusion tensor images of the mouse spinal cord. In *Proceedings of the conference on Visualization*, Research Triangle Park, North Carolina, USA, 1998.
- [58] M. Neeman, J. P. Freyer, and L. O. Sillerud. A simple method for obtaining cross-term free images for diffusion anisotropy studies in NMR microimaging. *Magn. Reson. Med.*, 21:138, 1991.
- [59] C. Pierpaoli and P. Basser. Toward a quantitative assessment of diffusion anisotropy. *Magn. Reson. Medicine*, 36:893, 1996.
- [60] S. Zhang, C. Demiral, and D. H. Laidlaw. Visualizing diffusion tensor MR images using streamtubes and streamsurfaces. *IEEE Trans. Visual Comput. Graphics*, 9:454, 2003.